Effect of lithium concentration on the network connectivity of nuclear waste glasses

Aine G. Black [a,b,*], Alex Scrimshire [c], Dinu Iuga [d], Yan Lavallée [e,f], Kate A. Morrison [b], Paul A. Bingham [c], Tracey Taylor [g], Laura Leay [a,h], Mike T. Harrison [g], Frédéric Blanc [b,i,j,*], Maulik K. Patel [a,*]

[a] Department of Materials, Design and Manufacturing, University of Liverpool, Liverpool L69 3GH, UK
[b] Department of Chemistry, University of Liverpool, Liverpool L69 7ZD, UK
[c] Materials and Engineering Research Institute, College of Business, Technology and Engineering, Sheffield Hallam University, Sheffield S1 1WB, UK
[d] Department of Physics, University of Warwick, Coventry CV4 7AL, UK
[e] Department of Earth and Environmental Sciences, Ludwig-Maximilians-Universität München, Munich, Germany
[f] School of Environmental Sciences, University of Liverpool, Liverpool L3 5DA, UK
[g] National Nuclear Laboratory, Central Laboratory, Sellafield, Cumbria CA20 1PG, UK
[h] National Nuclear Laboratory, Workington Laboratory, Havelock Road, Workington, Cumbria, CA14 3YQ, UK
[i] Stephenson Institute for Renewable Energy, University of Liverpool, Liverpool L69 7ZF, UK
[j] Leverhulme Research Centre for Functional Materials Design, University of Liverpool, Liverpool L7 3NY, UK

ARTICLE INFO

ABSTRACT

Structure of borosilicate glasses with varying Li_2O contents were investigated using Magic Angle Spinning (MAS) Nuclear Magnetic Resonance (NMR), employing ^6Li, ^{11}B, ^{23}Na, ^{27}Al and ^{29}Si nuclei. ^{11}B MAS NMR revealed that increasing Li_2O contents result in formation of $[BO_4]^-$ sites at the expense of BO_3. $^{11}B\{^6Li\}$ and $^{27}Al\{^6Li\}$ dipolar heteronuclear multiple quantum correlation (D-HMQC) NMR revealed Li as a charge compensator for anionic tetrahedral sites with increased Li. $^{11}B\{^6Li\}$ J-coupling mediated HMQC NMR suggested the possible association of Li with non-bridging oxygens on Q^2 and Q^3 sites, indicating its dual role in the glass network. ^{29}Si and ^{23}Na MAS NMR spectra showed depolymerisation of the silicate network and shortening of Na-O bond lengths with increased Li. NMR results are supported by Raman spectroscopy and thermal analysis that indicate depolymerisation of the silicate network and a reduction in glass transition temperature at higher Li content.

1. Introduction

The objective of radioactive waste packaging is to produce a passively safe wasteform by immobilisation or encapsulation. Immobilisation through vitrification to produce a glass wasteform is the process of choice in many countries, especially for high level waste (HLW) [1]. Vitrification is attractive as a large number of elements from the waste can be incorporated into the glass structure, which has high thermal stability and radiation tolerance, plus excellent durability in corrosive environments over prolonged periods of time [2,3]. HLW comprises of more than 30 different elements, many of which are radioactive with a range of half-lives from a few days to millions of years [4]. In the UK, it is planned that the vitrified HLW will be permanently disposed underground in a deep geological disposal facility (GDF) at depths of between 200 and 1000 m [5].

The borosilicate 'base' glasses studied in this work are 'Mixture Windscale' (MW, a 4-oxide glass) and 'Calcium Zinc' (CaZn, a 7-oxide glass) [2,6,7], which are used in the UK to vitrify HLW (see Table 1 for chemical compositions). Historically, the UK used the MW glass composition, but, more recently, CaZn glass has been developed to account for expected future changes in the HLW stream. This includes post-operational clean-out operations that will result in increased quantities of molybdate solids in the waste. The addition of CaO allows for the incorporation of higher Mo content in the glass network and preferential formation of powellite ($CaMoO_3$) which has very low aqueous solubility, as opposed to alkali molybdate phases which are, in contrast, highly soluble [8]. In formulating these borosilicate glasses, half of the Li_2O is removed as it is later added with the HLW feed as

LiNO$_3$. There, it acts as a flux to prevent the formation of refractory oxides in the calcination process that could potentially be hard to dissolve into the glass melt [2,9].

Li typically has a coordination of 4 or lower in silicate glasses [10] and can have two roles in the glass network: firstly, as a network modifier, where it breaks the covalent bonds between network formers and bridging oxygens (BOs), replacing them with weaker ionic bonds and creating non-bridging oxygens (NBOs), and secondly as a charge compensator where the Li ion will charge balance negatively charged structural units such as [BO$_4$]$^-$, as described [11–13]. The configuration and role taken by Li are governed by glass composition and total Li$_2$O in the system [14,15].

In three-component B$_2$O$_3$-SiO$_2$ borosilicate glasses, the addition of Na$_2$O results in the conversion of charge-neutral BO$_3$ sites to anionic [BO$_4$]$^-$ sites that will require charge balancing. With the progressive addition of Na$_2$O to the glass, NBOs begin to form initially in the silicate subnetwork and then in the borate subnetwork on the BO$_3$ sites, resulting in the depolymerisation of both [12,16–19]. In Li-Na-borosilicate glasses there is a preference for Li to primarily associate with the Si network and Na with the B network [20–22]. When the Li-Na-borosilicate glass network is saturated with silicate NBOs and [BO$_4$]$^-$ sites, increasing the Li content leads to the formation of additional NBOs on the BO$_3$ sites, resulting in further depolymerisation of this network [14,20,22,23]. Where Al is added to Na-borosilicate glasses the Al exists within tetrahedral coordinated sites ([AlO$_4$]$^-$) as a network former, thus it will be in competition with the anionic [BO$_4$]$^-$ sites for charge compensation by the alkali cations. This results in the conversion of [BO$_4$]$^-$ to BO$_3$ sites when Al is added to the network [18,24]. At low concentrations (< 5 wt%), ZnO in mixed alkali borosilicate glasses preferentially forms 4-coordinated [ZnO$_4$]$^{2-}$ units, which require charge compensation by Na$^+$ or Li$^+$ [25]; this results in a reduction of NBOs as Na/Li will take on the charge compensating role over modifying the network. [ZnO$_4$]$^{2-}$ acts as a network former, resulting in an increase in polymerisation as Si-O-Zn linkages are formed with SiO$_4$ tetrahedra [26,27]. When CaO is added to the glass network it has been reported that Ca^{2+} ions have an average coordination of 6 [28,29], although research using NMR spectroscopy have suggested that Ca^{2+} are mainly in 7- and 8-fold coordination sites [30]. Ca^{2+} ions take on the role of network modifier and due to their high cation field strength (CFS), the addition of CaO results in the formation of more NBOs in the network [31].

NMR spectroscopy has been pivotal to our understanding of glass networks because of its capability to assess short- and medium-range structures as well as local site motion from external and internal magnetic interactions [32,33]. More specifically, NMR enables access to the effect that chemical elements have on the connectivity and coordination of the glass structure [16]. A significant amount of work has particularly focused on the effect of CFS [17,34] and Na environment [35,36] in the glass network using ^{23}Na MAS NMR to correlate the shift and Na-O bond length with the modifier concentration. This was then expanded to include a wider range of network modifiers, such as Li and K, particularly investigating their site preferences from 1D and 2D ^{11}B and ^{17}O MAS NMR experiments [20]. The authors concluded that the differences observed in ^{11}B and ^{17}O shifts suggest significant differences between Li and Na/K preferences for coordination by BOs and NBOs where Li prefers NBOs, which may result in Li-silicate rich regions.

Previous experimental works have suggested, indirectly through line-shape analysis of 1D and 2D MAS NMR spectra of ^{11}B and ^{17}O, that the presence of Li in Na-borosilicate glasses creates NBOs on BO$_3$ sites and silicate tetrahedra, with a preference for silicates [20,37]. It is challenging to directly observe the association of Li with boron and NBOs in these glass compositions from 1D MAS NMR spectra, therefore complex 2D MAS NMR experiments are required. Supporting evidence is now presented from 2D MAS dipolar-coupling and J-coupling heteronuclear multiple quantum correlation (D-HMQC [38] and J-HMQC [39]) NMR spectroscopy experiments probing proximities between Li and B. In the work presented here we will show that Li$^+$ ions are in close proximity to BO$_3$ sites even at half lithium content for both MW and CaZn glasses, suggesting that for these glass compositions the formation of Si-NBOs occurs at a relatively low modifier content (as low as 2.2 mol % Li$_2$O). To the best of our knowledge, this close association of Li and BO$_3$/[BO$_4$]$^-$ sites has not previously been demonstrated directly in borosilicate glasses. The nature of the bonding and interactions between Li and both boron coordinations is not often remarked upon in the literature. From the work presented here enhanced information about the nature of Li BO$_3$ and Li [BO$_4$]$^-$ interactions is now available where it is suggested that Li BO$_3$ interactions are mediated via J-coupling (through bond) and dipolar coupling (through space) interactions whereas Li [BO$_4$]$^-$ associations are primarily mediated via dipolar coupling interactions. This provides further insight into the nature of the Li B interactions, coordination chemistry, and connectivity of the glass network.

The present work investigates the effects of Li content on the network connectivity of MW and CaZn base glasses by comparing experimental results for the half- and full-Li versions of these compositions. The glass compositions are herein referred to as MW ½Li, MW full-Li, CaZn ½Li and CaZn full-Li. Gaining an in-depth knowledge of the pristine base glass network will enable the prediction of long-term evolution in extreme environments of radiation and ground water leaching. While the role of Al, Zn and Ca is known in simple Na-Li-borosilicate glasses as described above, the correlated effect of Li concentration with network complexity is not yet understood. Similarities and differences between a 4-oxide and 7-oxide glass network have been obtained, enabling understanding of the role of Li in these glass networks and how it may change when complexity of the system is increased. Previous research on glasses with compositions of current interest focused on both their dissolution and long-term behaviours [22,26,40,41]. The previous studies carried out are very important as the glass compositions are intended for the immobilisation and disposal of HLW but an in-depth

Table 1

Nominal and measured compositions of glass samples in oxide mol%. Compositions were measured using ICP-OES for B and Li and XRF for all remaining oxides. The uncertainty noted in the measured values is for the cation. Al$_2$O$_3$ presence in the MW measured compositions is from crucible contamination, the very small amount of Fe$_2$O$_3$ is also from possible furnace or equipment contamination. Superscripts F and M indicate whether the cation is a network former and modifier, respectively.

Oxide Mol %	SiO$_2^F$	B$_2$O$_3^F$	Li$_2$O^M	Na$_2$O^M	Al$_2$O$_3^F$	CaO^M	ZnO^F	Fe$_2$O$_3$
				Nominal				
MW ½Li	63.33	20.00	5.55	11.12	-	-	-	-
MW full-Li	60.01	18.94	10.51	10.54	-	-	-	-
CaZn ½Li	50.83	21.56	4.52	8.85	2.64	6.86	4.73	-
CaZn full-Li	48.65	20.63	8.63	8.48	2.53	6.57	4.52	-
				Measured				
MW ½Li	65.27 ± 1.51	19.32 ± 0.60	4.56 ± 0.09	10.73 ± 0.41	0.13 ± 0.01	-	-	-
MW full-Li	60.08 ± 1.42	20.27 ± 0.64	9.35 ± 0.18	9.98 ± 0.39	0.25 ± 0.01	-	-	0.15 ± 0.01
CaZn ½Li	53.29 ± 1.18	20.35 ± 0.60	2.20 ± 0.04	8.24 ± 0.30	2.98 ± 0.13	7.61 ± 0.24	5.32 ± 0.27	-
CaZn full-Li	49.34 ± 1.10	21.62 ± 0.65	5.53 ± 0.10	7.67 ± 0.28	3.64 ± 0.16	7.23 ± 0.23	4.97 ± 0.26	-

knowledge of the structure of these glasses has yet to be developed. ^{11}B, ^{27}Al and ^{29}Si MAS NMR spectra have previously been obtained on compositions similar to the CaZn full-Li glass in this work [41], however, quantitative measurements are required to accurately study the connectivity of the glass network. To the best of our knowledge the work presented here is the first to fully compare the MW and CaZn compositions and the influence of Li content on their respective glass structures at the atomistic level, which is a critical step to enable future research aiming to quantify and understand the impact of radiation from HLW on the transient properties of these glasses.

2. Materials and methods

2.1. Sample preparation

All reagents held 99.9% purity and were oven dried at 393 K for 48 hours minimum prior to weighing and mixing, to remove moisture. All glasses were melted in alumina crucibles in 100 g batches. ½Li glasses were prepared using frit provided by the National Nuclear Laboratory (UK) that was fused in an electric muffle furnace at 1373 K (ramped at 10 K/min) for 3 hours; in the last 90 minutes the melt was stirred using a silica rod to ensure chemical homogeneity. Subsequently, the melts were annealed at 753 K for 3 hours and then allowed to cool to room temperature in the furnace at a rate of 10 K/min. The measured compositions of the frit are given in Table 1 and are representative for MW ½Li and CaZn ½Li. Full-Li glasses were fabricated through the addition of the appropriate quantity of Li_2CO_3 (a laboratory substitute for $LiNO_3$) to the respective ½Li frits.

The as-fabricated glass monoliths were reduced to fine powders by ball milling in an 8000D mixer/mill by SPEX SamplePrep, using a silicon nitride vial and ball media. The samples were milled at 1-minute intervals and the consistency of the glass powders were checked after each milling cycle. A maximum of 5 cycles was used until a fine powder was produced. The 1-minute interval between each cycle prevented local heating of the samples (temperature increases of around 30 °C have been observed when milling continuously for 5 minutes [42], much lower than the T_g of these glasses (Table 4)) .

2.2. Compositional analysis

The chemical compositions were analysed using Inductively Coupled Plasma Optical Emission Spectroscopy (ICP-OES) and X-Ray Fluorescence (XRF) Spectrometry and are tabulated in Table 1. ICP-OES was used to measure B and Li and all remaining oxides were measured using XRF. ICP-OES was carried out by the Sheffield Assay Office using a traditional microwave assisted digestion route using HNO_3, HCl and HF acids. For XRF analysis, samples were prepared into fused beads for XRF analysis. Samples were prepared by mixing 1 g of glass powder with 10 g of $Li_2B_4O_7$ doped with 0.5 % LiI (an anti-cracking agent). The mixture was then melted in a platinum crucible in a LeNeo automatic fusion system at 1338 K for 21 minutes and 45 s, then poured and cooled forming a homogenous fused bead. XRF analysis was then carried out by Glass Technology Services using a Bruker S4 Pioneer Wavelength dispersive XRF equipped with a Rh X-ray tube.

CHN combustion analysis was carried out on the glass powders after milling to ensure contamination did not occur, no nitrogen was detected in any composition (within the detection limit of 0.5 wt %), and furthermore no signal at -50 ppm (chemical shift of Si_3N_4 [43]) was observed in the ^{29}Si NMR spectra (Figure S1).

2.3. Nuclear magnetic resonance spectroscopy

[11]B (nuclear spin I = 3/2) MAS NMR spectra were recorded at four external magnetic fields: (i) a 400 MHz Bruker Avance III HD spectrometer with a 4 mm HXY Bruker probe (in double resonance mode) tuned to $\nu_0 = 128.38$ MHz and under a MAS rate of $\nu_r = 10$ kHz, (ii) a 500

MHz Bruker Avance NEO spectrometer with a 3.2 mm HXY or a HX Bruker probe tuned to $\nu_0 = 160.46$ MHz on X and under a MAS rate of 10 kHz, (iii) a 800 MHz Bruker NEO spectrometer equipped with a 1.9 mm HXY Tri gamma Bruker probe tuned to $\nu_0 = 256.71$ MHz on X and under an MAS rate of $\nu_r = 30$ kHz, and (iv) a 850 MHz Bruker NEO spectrometer equipped with a 3.2 mm HXY Bruker probe tuned to $\nu_0 = 272.76$ MHz for [11]B on X (and $\nu_0 = 125.11$ MHz for [6]Li on Y) under a MAS rate of $\nu_r = 20$ kHz. Samples were packed into either 1.9-, 3.2- or 4-mm zirconia Bruker rotors. Quantitative 1D spectra were obtained at 500 MHz using a one pulse sequence with a central transition (CT) selective π/2 pulse and 1D spectra at 400, 500 and 800 MHz were acquired using rotor-synchronised Hahn echo pulse sequence π/6 – τ – π/3 – τ – acq with τ corresponding to one rotor period. Pulses with short flip angles of π/6 (solid) of duration 0.83 μs and using rf field amplitude of $\nu_1 = 50$ kHz were used to ensure that full excitation was obtained [44]. A quantitative recycle delay of 50 s was used at 400, 500 and 800 MHz and found to be sufficiently long to allow for complete longitudinal relaxation. This corresponds to a delay longer than 5 × T_1 where T_1 is the spin-lattice relaxation time measured via a saturation recovery pulse sequence using a saturation block of 100 π/2 pulses separated by 1 ms. The resulting data were fit using the equation I(t) = I_0[1-exp(-(t/T_1)] where I(t) is the magnetization at time t, I_0 the initial magnetization and t the variable delay for magnetization build up. [11]B T_1 did not vary significantly with composition. Quantification of the boron sites was obtained from the one pulse spectra at 500 MHz. The probe boron background was removed in the one pulse ^{11}B MAS NMR spectra of the glasses by collecting 1D spectra of KBr (a sample containing no boron) under the exact same experimental conditions. Non quantitative [11]B spectra at 850 MHz were acquired using a one pulse sequence with CT selective π/2 pulses of duration 5 μs using field amplitude $\nu_1 = 50$ kHz and recycle delays of 5 s were used.

Experimental ^{11}B 1D MAS NMR spectra were fit using a second order quadrupolar line-shape for the BO_3 sites and a Gaussian distribution for the $[BO_4]^-$ sites as implemented in DMFit [45]. Quadrupolar parameters C_Q, η and δ_{iso} were extracted from the fits of the appropriate slices in the MAS dimension of the MQMAS spectra. C_Q defines the strength of the nuclear quadrupolar coupling to the surrounding electric field gradient [46], η is the asymmetry parameter ranging from 0 to 1 and δ_{iso} is the isotropic chemical shift (obtained from the MQMAS). These parameters could not be extracted very accurately for the $[BO_4]^-$ sites as they have very small C_Q values (in the range 0.2 to 0.4 MHz) due to their symmetrical nature thus are better represented by Gaussian line-shapes. The 1D [11]B MAS spectra were fit in DMFit using the parameters defining the line-shape by varying the signal intensity of each site to achieve a convergence of the fits at all three magnetic fields used. The spectra were fit independently 10 times to estimate the error in the fits.

2D triple quantum [11]B MQMAS [47] experiments were carried out at 400 and 500 MHz using a shifted echo [48,49] pulse sequence. A MAS rate of 8 kHz was used as a MAS rate of 10 kHz resulted in the BO_3 signal overlapping with a spinning sideband of the $[BO_4]^-$ site. A rf field amplitude of 100 kHz for the excitation (5.5–6 μs) and reconversion pulses (1.7–2 μs) and a rf field amplitude of 4–5 kHz for the soft π selective pulse (44–45 μs) were used with pulse durations being optimised at each magnetic field. 112 t_1 increments of incremental duration of 41.7 μs (3 rotor periods) each were collected with a recycle delay of 3.5 s and an echo delay of 5 ms. The [11]B isotropic chemical shift δ_{iso} (which is independent of the external magnetic field) is then obtained from the following Eq. (1):

$$\delta_{iso} = \frac{10}{27}\delta + \frac{17}{27}\delta_1 \qquad (Eq. 1)$$

where δ is the shift in the horizontal direct dimension (obtained from the centre of mass of each site when fit with the appropriate model as described below) and δ_1 is the isotropic shift in the vertical dimension.

Two different [11]B{[6]Li} ([6]Li I = 1) HMQC [39] experiments were

carried out; one with and one without a $SR4_1^2$ recoupling sequence [50]. The HMQC with the $SR4_1^2$ recoupling sequence is dipolar mediated known as a D-HMQC [38] and the HMQC without the recoupling is J-coupling mediated, called a J-HMQC. All HMQC spectra were acquired on a 850 MHz Bruker NEO spectrometer equipped with a 3.2 mm HXY Bruker probe tuned to $\nu_0 = 272.76$ MHz for ^{11}B and $\nu_0 = 125.11$ MHz for ^6Li under a MAS rate of $\nu_r = 20$ kHz. Pulses of rf field amplitude of 50 and 125 kHz with $\pi/2$ pulse of durations of 5 and 2–3 μs were used for ^{11}B and ^6Li, respectively. Pulse durations were optimised for maximum signal and the pulse on the ^{11}B nucleus is central transition selective. A recycle delay of 8 s was used and 512 and 256 scans were used for the J- and D-HMQC, respectively. A double frequency sweep (DFS) [51] of 2 ms at a 35 kHz rf field amplitude achieving a gain of approximately 2 was used to increase the signal-to-noise ratio (SNR). For the J-HMQC, recoupling times were optimised for each sample and were found to yield the highest sensitivity for 2 ms for the full-Li samples and 4 ms for CaZn ½Li. Recoupling times of 2, 4 and 8 ms were trialled for MW ½Li. 60 t_1 increments were rotor-synchronised with the MAS rate. These J-HMQC experiments were performed slightly off magic angle (approx. 1°) to increase the coherence lifetime of the half integer ^{11}B quadrupolar nucleus [52]. For the D-HMQC a recoupling pulse with a rf field of 80 kHz and duration 1.2 ms was used for all compositions with 80 rotor-synchronised t_1 increments. Note here that due to probe tuning limitations on nuclei with close Larmor frequencies to ^{11}B ($\nu_0 = 272.76$ MHz), ^6Li ($\nu_0 = 125.11$ MHz) was used instead of the higher natural abundance nucleus ^7Li ($\nu_0 = 330.39$ MHz).

^6Li MAS NMR spectra were obtained using a one pulse sequence with a $\pi/2$ flip angle of duration 2 μs with a rf field amplitude of 125 kHz with a non-quantitative recycle delay of 1300 s at 850 MHz. The ^6Li T_1 was measured to be 1100 s at 800 MHz on the MW ½Li sample using the same approach as detailed for ^{11}B above and it is expected the ^6Li T_1 value for the other compositions to be within the same order of magnitude.

^7Li static NMR spectra at room temperature were acquired on a 400 MHz Bruker Avance III HD spectrometer equipped with a 4 mm HXY Bruker probe (in double resonance mode) tuned to $\nu_0 = 155.51$ MHz and using a $\pi/2$ pulse of duration 1.5 μs with a rf field amplitude of 83 kHz. Data were acquired using quantitative recycle delays of five times T_1 determined using the same approach detailed above for ^{11}B nuclei.

$^{27}Al\{^6Li\}$ (^{27}Al I = 5/2) D-HMQC with $SR4_1^2$ recoupling spectra were obtained with the same experimental set up as described above for ^{11}B $\{^6Li\}$ D-HMQC, however with the X channel tuned to $\nu_0 = 221.52$ MHz for ^{27}Al detection. Pulses of rf field amplitude of 50 kHz with $\pi/2$ CT selective pulse durations of 5 μs was used for ^{27}Al and the same rf field was used for ^6Li as described above. A recoupling pulse with a rf field amplitude of 80 kHz was used for all compositions with a recoupling duration of 6 ms. 512 scans, 80 rotor-synchronised t_1 increments and a recycle delay of 0.7 s were used. A DFS block of 2 ms at a 25 kHz rf field was used providing a sensitivity gain of approx. 3.

CT selective ^{27}Al MAS NMR spectra were obtained using a one pulse sequence with a $\pi/2$ flip angle of duration 5 μs with a rf field amplitude of 50 kHz with a delay of 1 s at 850 MHz. The ^{27}Al T_1 was measured to be 0.5 s at 400 MHz using the same approach detailed above for ^{11}B nuclei.

^{29}Si (I = 1/2) MAS NMR spectra were obtained on a 400 MHz Bruker Avance III HD spectrometer with a 4 mm HXY Bruker probe (in double resonance mode) tuned to $\nu_0 = 79.50$ MHz and under a MAS rate of $\nu_r = 8$ kHz. Samples were packed into 4 mm zirconia Bruker rotors. A one pulse sequence with a $\pi/2$ flip angle pulse of duration 5 μs with a rf field amplitude of 50 kHz was used with a sample dependent quantitative recycle delay ranging from 1500 to 4500 s. These delay times correspond to a delay longer than five times T_1 which was determined via a saturation recovery pulse sequence as described above and the resulting data were fit with a stretch exponential equation $I(t) = I_0[1-exp(-(t/T_1)^\alpha)]$ where α is the stretch exponent. The low α value obtained experimentally (0.6 or below in this work) correlates to a large distribution of correlation times and a wide distribution of bond angles which

is expected given the amorphous nature of the glasses.

^{23}Na (I = 3/2) MAS NMR spectra were recorded on an 800 MHz Bruker NEO spectrometer equipped with a 1.9 mm HXY Tri gamma Bruker probe tuned to $\nu_0 = 211.65$ MHz under a MAS rate of $\nu_r = 30$ kHz and on a 400 MHz Bruker Avance III HD spectrometer with a 4 mm HXY Bruker probe (in double resonance mode) tuned to $\nu_0 = 105.84$ MHz and under a MAS rate of $\nu_r = 10$ kHz. Samples were packed into either 1.9 or 4.0 mm zirconia Bruker rotors. At both fields, a one pulse spectra with a short flip angle of $\pi/6$ (solid) of duration 1.04 μs with a rf field amplitude of 40 kHz were used to ensure that full excitation was achieved. A quantitative recycle delay of 10 s was found to be sufficiently long to allow for complete longitudinal relaxation determined from T_1 measurements following the same approach as detailed above for ^{11}B nuclei.

^{11}B, ^6Li, ^{29}Si, ^{23}Na and ^{27}Al (chemical) shifts were referenced externally to the field-independent $NaBH_4$ signal at -41.4 ppm that corresponds to the primary reference BF_3Et_2O resonating at 0 ppm [53], 1 M LiCl in H_2O at 0 ppm, the M site of Q8M8 at 11.5 ppm [54] that corresponds to the primary reference Me_4Si at 0 ppm, 1 M NaCl in H_2O at 0 ppm and 0.1 M $Al(NO_3)_3$ in H_2O, respectively. References were also used for rf field amplitude calibrations.

2.4. Raman spectroscopy

Raman spectroscopy was performed using a Reinshaw InViaTM Qontor® Confocal Raman imaging microscope equipped with a 532 nm laser. Spectra were acquired in the range 200–2000 cm^{-1} using a Master Centrus CCD detector and grating set to 2400 lines/mm using a 50 × objective lens. The background signal was corrected using the software OriginPro (OriginLab Corporation, version 2020b). To obtain a high SNR, 30 accumulations of 15 seconds each were acquired with laser power at 50 percent to ensure the laser did not mark the sample surface. The Q^n region of each of the Raman spectra were fitted using Gaussian line-shapes to well-established Raman modes where the full width half maximum (FWHM) and intensity are unconstrained values. Spectra were fit independently 5 times to obtain the error.

2.5. Thermal analysis

The glass transition temperature (T_g) of the glass powders was obtained by differential scanning calorimetry (DSC) using a Netzsch STA (Simultaneous Thermal Analyser) 449 F1 Jupiter®. For these measurements a two-step process was utilized: 1) the sample assembly (*i.e.*, empty sample and reference Pt crucibles (with lids), sitting on a Pt sample holder) was heated to temperature in an argon atmosphere to constrain the calorimetric signature of the system; subsequently, 2) the sample crucible was loaded with 50 mg of glass powder and the sample assembly was subjected to the same thermal profile as in step 1. This two-step process was conducted for every glass sample. The DSC temperature program heated from room temperature to 873 K (to obtain a relaxed melt), then cooled to 693 K (to lock in a glass structure at a known rate), heated again to 873 K (to monitor relaxation at a known cooling/heating rate), and finally cooled to room temperature; all segments at a rate of 10 K/min. The maximum temperature of 873 K was chosen as T_g is met at around 723–823 K (depending on chemistry and heating rate) and crystallisation initiates above 923 K. After the measurements, visual inspection suggested the absence of reaction between the samples and the platinum crucible. T_g is characterised by an endothermic inflection and was determined from the second DSC heating curve using the tangent and inflection line method, the standard method established by the International Confederation for Thermal Analysis [55]. The errors were calculated by plotting the line of worst fit for both the tangent and inflection lines.

3. Results

3.1. NMR

The ^{11}B MAS NMR of the four glass compositions obtained at 400, 500 and 800 MHz (Fig. 1) revealed two main signals that are observed at around 15 and 0 ppm and assigned to BO_3 and $[BO_4]^-$ sites, respectively. The signal from the BO_3 coordination is broader (approx. 3 kHz at 400 MHz) than that of the $[BO_4]^-$ coordination (approx. 1 kHz at 400 MHz) due to the higher symmetry of the latter significantly reducing the quadrupolar broadening. At 400 MHz, there is a significant overlap of the BO_3 and $[BO_4]^-$ resonances, challenging their full deconvolution,

however, at a higher field of 500 and 800 MHz, there is an important reduction of the NMR linewidth of the broader BO_3 site. This stems from a reduction of the relatively large second order quadrupolar anisotropic broadening for this site, that is not fully averaged out by MAS for this half-integer spin 3/2 nucleus and is inversely proportional to the magnetic field strength. In particular, at 500 MHz, the second order quadrupolar line-shape of the BO_3 sites is well resolved as previously observed in the literature [56,57].

The presence of multiple BO_3 and $[BO_4]^-$ sites was revealed from 2D ^{11}B MQMAS experiments at 400 MHz (Figs. 2 and 3) and 500 MHz (Figures S3 and S4) which yield isotropic spectra by removing the residual second order quadrupolar broadening that is not removed simply
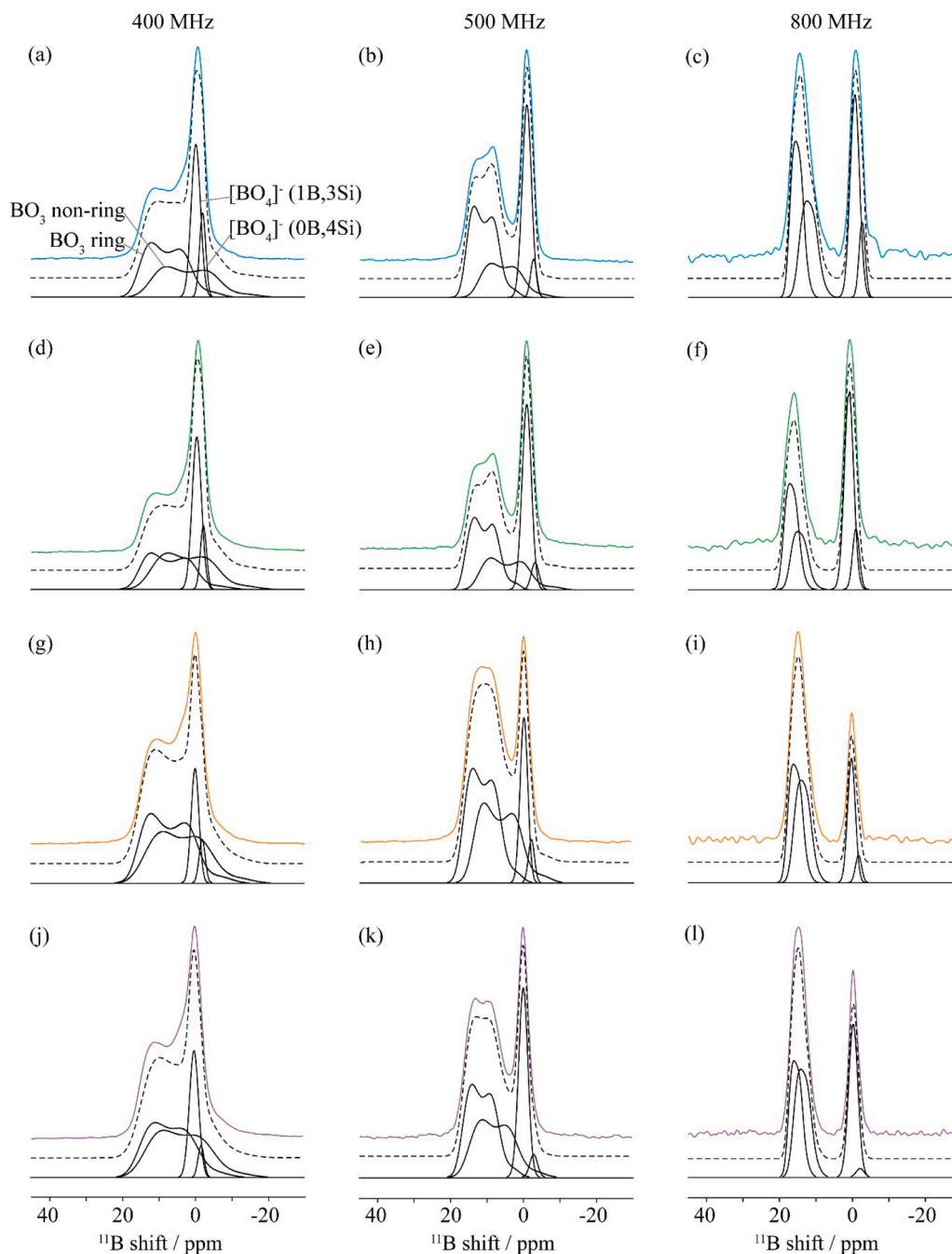
Fig. 1. Deconvolution of the ^{11}B MAS NMR Hahn echo spectra of (a-c) MW ½Li (blue), (d-f) MW full-Li (green), (g-i) CaZn ½Li (orange) and (j-l) CaZn full-Li (green) glasses at 400, 500 and 800 MHz based on the ^{11}B MQMAS data. The coloured lines are the experimental spectra that follow the same colour scheme for each composition throughout this work, the dashed black lines are the total fit using the appropriate models for each site as detailed in Section 2.3, and the BO_3 ring and non-ring and $[BO_4]^-$ (0B,4Si) and (1B,3Si) sites, are represented by solid black lines. Only spectra (a) are labelled but (b-l) follow the same labelling.

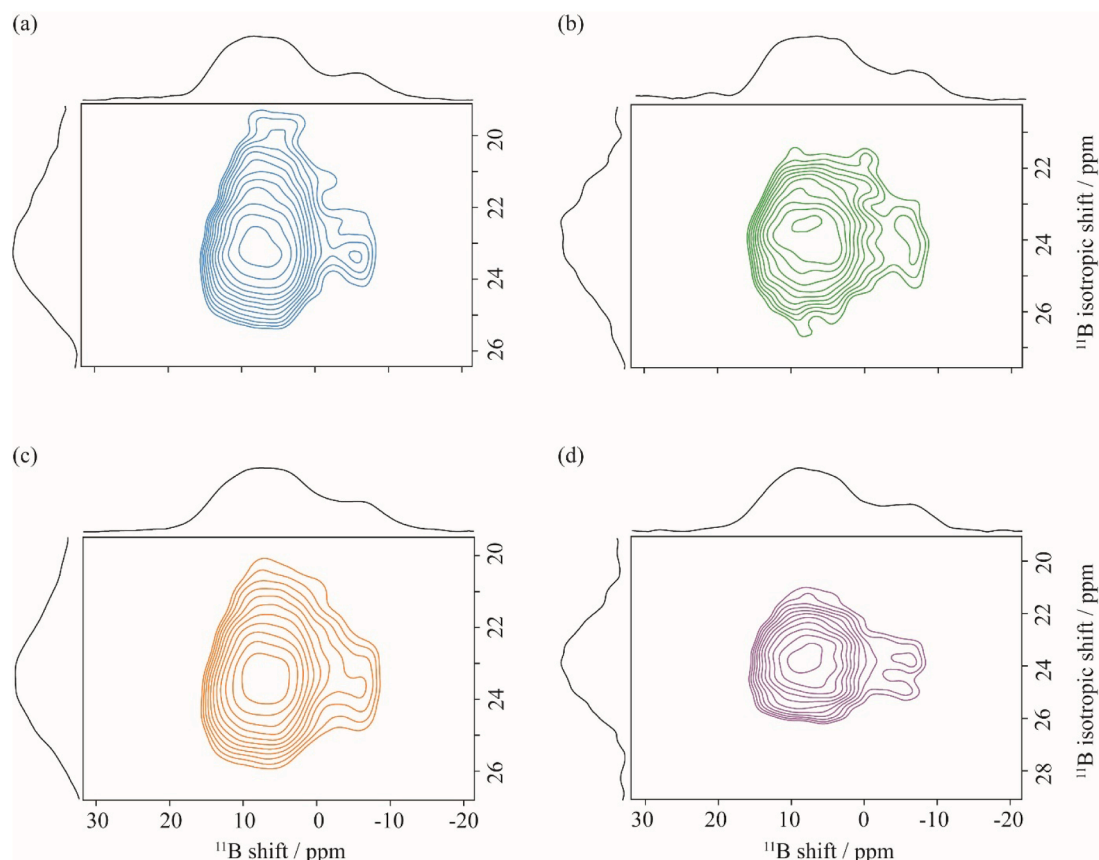**Fig. 2.** ^{11}B MQMAS of the BO$_3$ sites in (a) MW ½Li (blue), (b) MW full-Li (green), (c) CaZn ½Li (orange) and (d) CaZn full-Li (purple) glasses at 400 MHz. Horizontal spectra are the internal projections in the MAS dimension. Vertical spectra are the isotropic internal projections. The internal projections are only from data shown in the window of the spectral range displayed.

under MAS. This allows the various site contributions of the BO$_3$ and [BO$_4$]$^-$ signals to be observed. The 2D MQMAS spectrum of the BO$_3$ signal (Fig. 2) exhibits that, at least, two different BO$_3$ sites are present and correspond to well-known contributions from ring and non-ring BO$_3$ sites [21,58]. The signal observed at an δ_{iso} of 17–18 ppm is attributed to the BO$_3$ ring which is a central boron surrounded by oxygen bonds in rings [21]. The other signal detected at a δ_{iso} of 15–16 ppm corresponds to the BO$_3$ non-ring, a central boron surrounded by three oxygens typically distributed in the silicate units. Previous work looked at the distribution of the ring and non-ring BO$_3$ sites throughout the glass network using ^{11}B and ^{17}O MAS NMR [21] where it was suggested that the slight change in ^{11}B δ_{iso} of the non-ring BO$_3$ sites with increasing modifier content observed is due to the increased mixing of these sites with other components, such as silicon, in the glass network. The change observed in the ^{11}B δ_{iso} of the non-ring BO$_3$ in these glasses is within experimental error, perhaps suggesting less mixing of these sites in the glass compositions studied here. The SNR achieved was sufficiently high to obtain the relevant quadrupolar parameters, C$_Q$, δ_{iso} and η from fitting the ^{11}B MQMAS slices (Figures S5-S8) and were used in the fitting of the 1D ^{11}B MAS NMR spectra (Fig. 2 and S3).

It is clear from the 2D ^{11}B MQMAS experiments that there is a strong similarity in the quadrupolar parameters (Table 2, see below) of these ring and non-ring BO$_3$ sites causing large signal overlap, as experimentally observed (for example, the ^{11}B MAS NMR spectra at 400 MHz in Fig. 1). The key observable difference between the ring and non-ring sites is the presence of a horn in the quadrupolar line-shape of the BO$_3$ non-ring site due to the large C$_Q$ value of this site (approx. 3 MHz compared to 2.6 MHz for ring BO$_3$). It is expected that the non-ring BO$_3$ site will have a larger C$_Q$ than the ring BO$_3$ sites due to increased ordering around ring BO$_3$. It should be noted that the C$_Q$ of BO$_3$ sites in

borates and borosilicate is typically within the range 2.4–2.9 MHz in the literature [21,58–62] while in this work, C$_Q$ values of 2.9–3.2 MHz were obtained for the BO$_3$ non-ring sites in each composition. Whilst slightly larger, these values are still approximately within experimental error of the reported literature range and may suggest an increase in disorder of non-ring BO$_3$ sites in these glasses. This large C$_Q$ value is evidenced in Figs. 2, S5 and S7, where a discontinuity at -5 ppm is observed which is part of the low frequency horn of the second order quadrupolar line-shape of the non-ring BO$_3$ site. This horn is more evident at 400 MHz rather than 500 MHz due to greater quadrupolar broadening at a smaller magnetic field, Figures S5 and S7.

The fitting of the internal projection at 400 MHz is in excellent agreement with the experimental spectra (Figure S5), the same quadrupolar parameters (Table 2) were then used to fit the 500 MHz spectra producing also producing an agreeable fit (Figure S7).

The 2D MQMAS spectra of the [BO$_4$]$^-$ sites in these glasses are given in Fig. 3. The 2D ^{11}B MQMAS of the [BO$_4$]$^-$ sites show signals spread in an elongated line along the +1 diagonal that is typical of a distribution of shifts and is not observed for the BO$_3$ sites. This likely results from a line-shape for the [BO$_4$]$^-$ sites that is not dominated by the quadrupolar interaction given the small C$_Q$ values and for which the NMR parameters are very similar, resulting in a lack of resolution between the two [BO$_4$]$^-$ sites. However, it is evident from the fittings and slices taken in the isotropic dimension of the MQMAS (Figure S6) that there are at least two [BO$_4$]$^-$ sites present in each of the glasses: one at an δ_{iso} ranging from -2 to -1 ppm attributed to [BO$_4$]$^-$ (0B,4Si) sites in reedmergnerite (NaBSi$_3$O$_8$) type units and the other at an δ_{iso} of 0 to -1 ppm assigned to [BO$_4$]$^-$ (1B,3Si) sites in danburite (CaB$_2$Si$_2$O$_8$) type units [21]. The replacement of one silicon next-nearest-neighbour with one boron results in a small deshielding effect of about 2 ppm of the central boron atom.
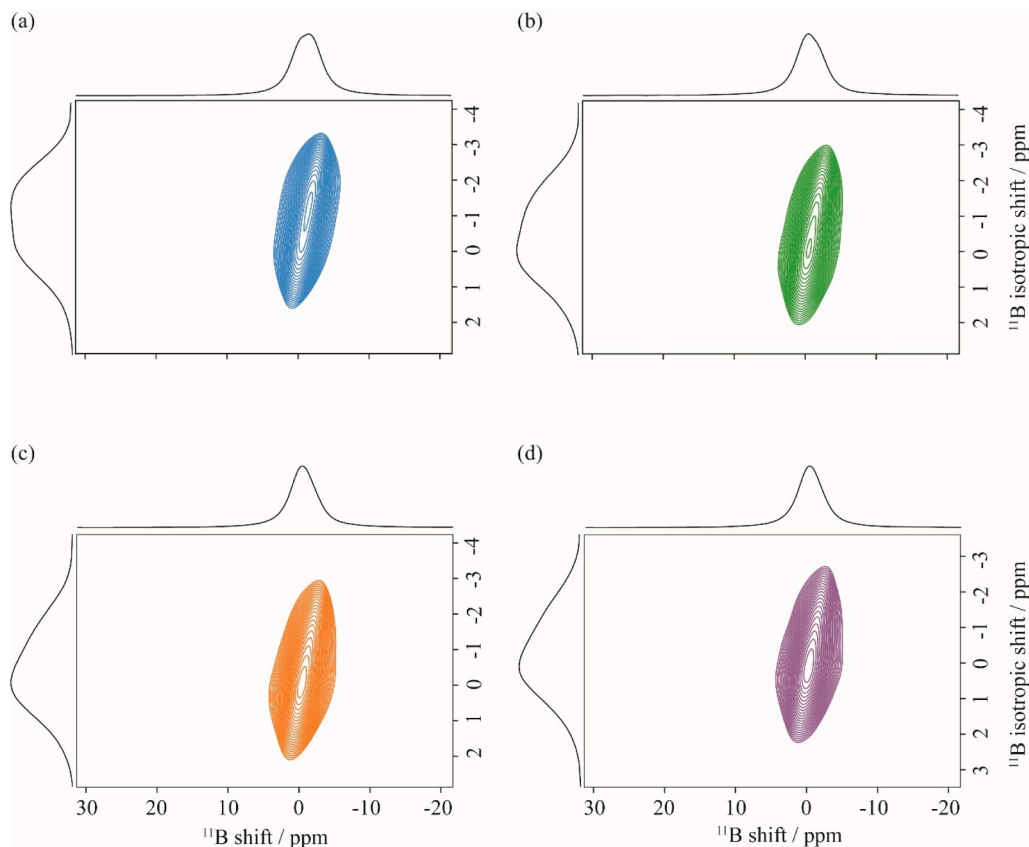
Fig. 3. ^{11}B MQMAS of the [BO$_4$]$^-$ sites in (a) MW ½Li (blue), (b) MW full-Li (green), (c) CaZn ½Li (orange) and (d) CaZn full-Li (purple) glasses at 400 MHz. Horizontal spectra are the internal projections in the MAS dimension. Vertical spectra are the isotropic internal projections. The internal projections are only from data shown in the window of the spectral range displayed.

The ^{11}B 1D MAS spectra in Fig. 1 were fit using a second order quadrupolar line-shape (BO$_3$ sites) and a Gaussian distribution ([BO$_4$]$^-$ sites) contributions from the four sites outlined above and accurately reproduce the experimental line-shapes, enabling the percentage contribution from each site to be obtained given that the area under each peak is proportional to the number of atoms: these are reported in Table 2. The total percentage of BO$_3$ to [BO$_4$]$^-$ structural units changes with composition, as expected based on literature [20,24,57,63,64]. In general, there is a larger population of BO$_3$ units compared to [BO$_4$]$^-$ in the glass network of CaZn than MW, which is expected due to the addition of aluminium and zinc to the CaZn glass network (Table 1). In CaZn glass, Al and Zn assume tetrahedral coordination [25,65]; [AlO$_4$]$^-$ and [ZnO$_4$]$^{2-}$ units compete with [BO$_4$]$^-$ units for charge compensation by modifier ions resulting in the transformation of [BO$_4$]$^-$ into BO$_3$ structural units and borate network depolymerisation. Comparing the full-Li glasses to the ½Li glasses, the percentage of BO$_3$ units converted to [BO$_4$]$^-$ units is less for MW glass (4 %, Table 2) than for CaZn glass (8 %), thus indicating that Li has more of an impact with increasing complexity of the glass network. Furthermore, Table 2 suggests that for the MW glass with increased Li content, the population of BO$_3$ ring and non-ring sites is largely similar as an approximate 3 % decrease is observed for both. This is not the case for the CaZn glass, where the difference in BO$_3$ ring and non-ring sites is greater as an approximate 5 and 3 % decrease in ring and non-ring BO$_3$, respectively, is observed. This effect could be due to the larger proportion of BO$_3$ in the CaZn composition resulting in greater BO$_3$ to [BO$_4$]$^-$ conversion upon lithium addition. Both compositions experience a decrease in [BO$_4$]$^-$ (0B,4Si) sites upon an increase in lithium content, from 18 to 11 % in MW glass and from 7 to 4 % in the CaZn. This contrasts with the increase in [BO$_4$]$^-$ (1B,3Si) sites observed, from 42 to 54 % in MW and from 28 to 39 % in

CaZn. This suggests that at higher lithium contents there is enhanced silicon and boron mixing, although there is no significant change in δ_{iso} of these sites upon lithium addition.

The ^{23}Na MAS NMR spectra for each glass at 800 MHz (Fig. 4) and 400 MHz (Figure S9) exhibit a single broad peak at around -10 ppm that is characteristic of Na cations in borosilicate glasses [66]. At 400 MHz, the line-shapes are asymmetric and possess a quadrupolar tail at lower frequency due to a large distribution of quadrupolar parameters. This is not observed at a higher field of 800 MHz as the second order quadrupolar anisotropic broadening is further reduced. ^{23}Na MAS NMR spectra at both fields were fit using a Czjzek distribution [67] in DMFit (Figure S10) with $\sqrt{\langle P_Q^2 \rangle}$ values of 2.5–2.7 MHz, where P_Q is the quadrupolar product [68,69] and δ of -7 ppm (for full Li samples) and -9 ppm for (half Li samples), typical for Na borosilicate glasses [70]. This model produces fits that are extremely agreeable with the experimental spectra at 400 MHz however it is clear that the spectra at 800 MHz cannot be fit using the same parameters. If the distribution of Na in the glass could be described using a Czjzek model, then the fits should be in good agreement at both fields with the same set of parameters. This suggests that the Na$^+$ ions in these glass compositions do not follow a Czjzek distribution and thus do not have a random Gaussian distribution as is assumed by the Czjzek model.

The ^{23}Na MAS NMR spectra at 800 MHz highlight that as the Li content is increased, for both MW and CaZn glasses, there is a change in centre of gravity of the peak to a higher frequency, an effect that is not noticeable at 400 MHz. This change in the ^{23}Na shift has been widely reported in the literature for glasses containing Na [24,70,71], stating that the ^{23}Na NMR shift exhibits an inverse relation with the average Na-O bond length. Therefore, according to this relationship, the increase

Table 2

^{11}B NMR parameters for MW and CaZn full-Li and ½Li glasses obtained from the MAS spectra. δ_{iso} is the isotropic chemical shift calculated from Eq. 1, η is the asymmetry parameter and C_Q the quadrupolar coupling constant, all obtained from fitting the BO₃ sites with a second order quadrupolar line-shape as described in the Materials and Methods Section 2.3.

Coordination	δ_{iso} (±1.0) / ppm	η (±0.1)	C_Q (±0.2) / MHz	Relative percentage (±3) / %
MW ½Li				
BO₃ ring	17.0	0.3	2.6	20
BO₃ non-ring	15.0	0.3	3.2	20
[BO₄]⁻ (0B,4Si)	-2.0	_[a]	_[a]	18
[BO₄]⁻ (1B,3Si)	0.0	_[a]	_[a]	42
MW full-Li				
BO₃ ring	18.0	0.2	2.6	18
BO₃ non-ring	15.0	0.3	3.2	17
[BO₄]⁻ (0B,4Si)	-2.0	_[a]	_[a]	11
[BO₄]⁻ (1B,3Si)	0.0	_[a]	_[a]	54
CaZn ½Li				
BO₃ ring	18.0	0.3	2.7	31
BO₃ non-ring	16.0	0.2	3.1	34
[BO₄]⁻ (0B,4Si)	-2.0	_[a]	_[a]	7
[BO₄]⁻ (1B,3Si)	0.0	_[a]	_[a]	28
CaZn full-Li				
BO₃ ring	18.0	0.3	2.7	26
BO₃ non-ring	16.0	0.2	2.9	31
[BO₄]⁻ (0B,4Si)	-1.0	_[a]	_[a]	4
[BO₄]⁻ (1B,3Si)	0.0	_[a]	_[a]	39

[a] Not determined due to the Gaussian line-shape experimentally observed.
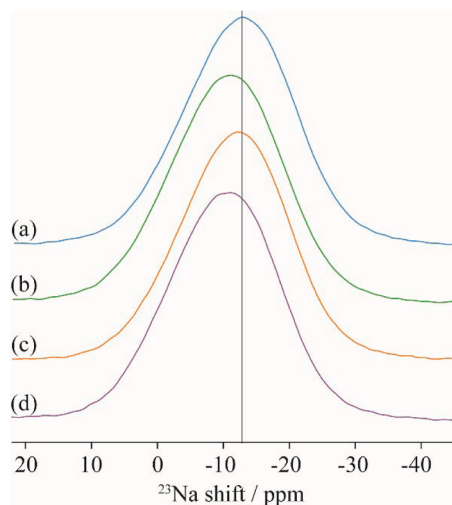
Fig. 4. Experimental ^{23}Na MAS NMR spectra at 800 MHz for (a) MW ½Li (blue), (b) MW full-Li (green), (c) CaZn ½Li (orange) and (d) CaZn full-Li (purple). Solid vertical line is used as a guide to the eyes to show the change in shifts (or its absence).

in Li results in a small decrease in Na-O bond length in a MW and CaZn glass. Comparing the ^{23}Na MAS NMR spectra of MW and CaZn for a given Li content appears to indicate no change in the Na-O bond length between these two networks. It is likely that the influence of Al and Zn on Na distribution is too small to observe, given the [23]Na signal broadening and relatively low Al₂O₃/ZnO concentration (Table 1).

Quantitative ^{29}Si MAS NMR spectra for each glass are displayed in Fig. 5. The resonances are broad (approx. 4 kHz), centred around -100 ppm, appear featureless, and are characteristic of amorphous silicates [72]. The broadening likely arises from the overlapping of chemical shifts from the various silicate linkages throughout the glass network (Qⁿ species where n denotes the number of bridging oxygens

surrounding the central silicon atom [25,63], Si-O-Si, Si-O-Al, Si-O-B, Si-O-Zn) resulting in a distribution of Si-O distances and O-Si-O angles [24,73]. Mean isotropic chemical shifts of Q², Q³ and Q⁴ units are typically at -85, -95 and -110 ppm, respectively, which show a trend towards a less shielded central silicon as the number of Si-O-Si per tetrahedron decreases [72–75]. Spectra are largely symmetrical, suggesting a wide distribution of bond angles throughout the silicate subnetwork. Despite the significant overlaps, an increase in chemical shift with the addition of Li to the glass network is observed and captures a gradual change from Q⁴ to Q³ units that is indicative of silicate subnetwork depolymerisation [71,72]. This is likely due to Li acting as a network modifier in the silicate subnetwork, which results in the breaking of Si-BO bonds in favour of the formation Si-NBO bonds. The centre of gravity of the ^{29}Si MAS NMR spectra are greater for both the CaZn glasses (at approximate [29]Si chemical shifts of -93 ppm for full-Li and -98 ppm for ½Li) compared to the MW glasses (-100 ppm and -105 ppm for the full-Li and ½Li), suggesting that CaZn glass contains more Si-NBO bonds and thus more Q² and Q³ units than MW glass. This change in polymerisation cannot solely be attributed to an increase in Li or the overall total modifier content as the network former and modifier contents are roughly the same for each class of glass (Table 1). This instead implies that the role of Li in the MW and CaZn silicate subnetworks is different, likely due to the increased complexity of the CaZn glass. This could be due to the presence of Al and Zn in the CaZn glass, which decreases the effective modifier concentration as more alkalis will be involved in charge compensation of these negatively charged structural units, [AlO₄]⁻ and [ZnO₄]²⁻ [76]. Furthermore, the addition of Al and Zn also results in the formation of Si-O-Al and Si-O-Zn linkages at the expense of Si-O-Si which will lower the Q⁴ fraction of the glass network [24,25].

[29]Si T_1 values were determined from saturation recovery build-up curves (Figure S11), as described in the Materials and Methods Section, to determine the effect of the Li content on the dynamics of the silicate subnetwork, when applicable. The pathway for [29]Si nuclear spins relaxation in glass is often driven by the coupling of the mobile quadrupolar alkali nuclei with [29]Si [77–79]. For the CaZn glass composition, as the Li content of the glass is increased, the T_1 values decreased which is likely due to a more efficient quadrupolar relaxation mechanism between the [29]Si nuclear spins with [7]Li (the quadrupolar and dominant NMR isotope of Li) [79] and [23]Na (also a quadrupolar nucleus). The T_1 reduction coincides with an increase in depolymerisation of the silicate subnetwork and the ^{23}Na MAS NMR spectra suggests at higher lithium contents the Na-O bond length has shortened. Thus, the
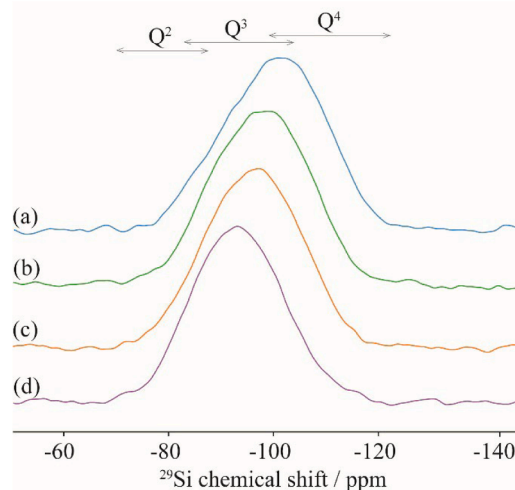

Fig. 5. Experimental ^{29}Si MAS NMR spectra at 400 MHz for (a) MW ½Li (blue), (b) MW full-Li (green), (c) CaZn ½Li (orange) and (d) CaZn full-Li (purple). Typical [29]Si Q², Q³ and Q⁴ chemical shift ranges are shown above the spectra.

reduction in T_1 for CaZn is likely a combination of Na^+ and Li^+ ions charge balancing the NBOs formed on the Q^2 and Q^3 units in the silicate network at increased lithium contents. It is worth noting that for the MW glass composition, the contribution of the Li content to ^{29}Si T_1 relaxation cannot be determined because of presence of a small amount of Fe_2O_3 impurity in the MW full-Li (Table 1) which introduces strong paramagnetic relaxation [80].

To probe the network connectivity and Li B interactions in these complex borosilicate glasses, two-dimensional multinuclear $^{11}B\{^6Li\}$ J-HMQC MAS spectra were obtained (Fig. 6). This experiment, was performed slightly off the magic angle setting to make use of both the isotropic part of the scalar J-coupling tensor that does not vanish under MAS and residual through-space dipolar coupling interaction, enabling high-resolution two-dimensional spectra between two quadrupolar nuclei close in space and mediated by J-coupling to be obtained [39,81]. The implemented J-HMQC sequence leads to two-dimensional spectra correlating the ^{11}B spectrum (which is detected directly because of its high sensitivity) with the indirectly observed ^6Li spectrum. This experiment allows one to investigate the association of ^{11}B with ^6Li in the glass network. The corresponding $^{11}B\{^6Li\}$ J-HMQC MAS spectra for the CaZn glasses at both Li contents and MW ½Li glass present correlations between the BO_3 signals (at 15 ppm as discussed previously) and the Li resonances (at 0 ppm, 1D MAS spectra in Figure S12) demonstrating spatial proximity between Li and BO_3 sites. Despite our best efforts, any potential correlation between Li and BO_3 in MW ½Li (Fig. 6a) could not be observed using a J-HMQC experiment. This MW ½Li glass possesses more Li than CaZn ½Li and similar Li content to CaZn full-Li (Table 1) for which correlations signals are observed. This implies that there is sufficient lithium in these glasses to detect the possible ^6Li and $BO_3/[BO_4]^-$ correlations but perhaps there are such a small number of Li BO_3 correlations in MW ½Li which detection is challenged by low natural abundance of ^6Li (~ 8 %). It may be possible to observe such interactions in double resonance $^7Li/^{11}B$ NMR experiments, but this probe configuration is inaccessible in our experimental setup. These results are

consistent with those from ^{11}B MAS NMR where it was found that lithium has a greater influence on the 7-oxide network as opposed to the 4-oxide.

The close proximity of Li to BO_3 could possibly be due to the presence of NBOs on these sites and Li acting as charge compensator, as the literature suggests that NBOs do form on BO_3 sites upon the addition of network modifier cations [12,14,18,82]. However, if that were the case it would be evident from the quadrupolar parameters extracted from fitting the 2D MQMAS spectra. If NBOs were present on the BO_3 sites a large η value in the range 0.5–0.8 would be obtained [83] or an increase in the ^{11}B isotropic chemical shift of these sites would be seen [59], none of which is observed (Table 2). A C_Q value larger than typical literature values is observed for all BO_3 non-ring sites (Table 2), however a large C_Q is not necessarily analogous with the presence of NBOs. Instead, the proximity of Li to BO_3 could be due to BO_3 non-ring sites being typically distributed in the silicate network [20,21]. From the literature on borosilicate glasses, Li has a preference to associate with the silicate network due to the presence of NBOs on Q^n tetrahedra [20], and from the ^{29}Si NMR spectra shown above it was observed that upon lithium addition depolymerisation of the silicate network occurs creating more NBOs in the silicate network. Thus, the correlation signal observed in Fig. 6 is possibly due to the bonding of BO_3 non-ring sites to Q^3 and Q^2 tetrahedra where Li is acting as charge compensator to the NBOs on these sites. Additionally, the percentage of $[BO_4]^-$ (1B, 3Si) sites (Table 2) demonstrates there is a large degree of silicon-boron bonding as this is the most abundant of the four boron coordinations in three of the compositions. It should be noted that the ^7Li static NMR spectra at room temperature (Figure S13) are broad (full-width at half maximum $\omega/2\pi$ of ~ 4.5 kHz for the ½Li compositions and ~ 5 kHz for the full-Li compositions) arising from the strong ^7Li ^7Li homonuclear dipolar coupling interaction. This indicates that the Li ion jump rates (τ^{-1}) are slow compared to $\omega/2\pi$, i.e., $\tau^{-1} < \omega/2\pi$, therefore the mobility of Li ions at room temperature is not significant to these glasses. Furthermore, the correlation signals between ^6Li and ^{11}B in Figs. 6 and 7 are slightly
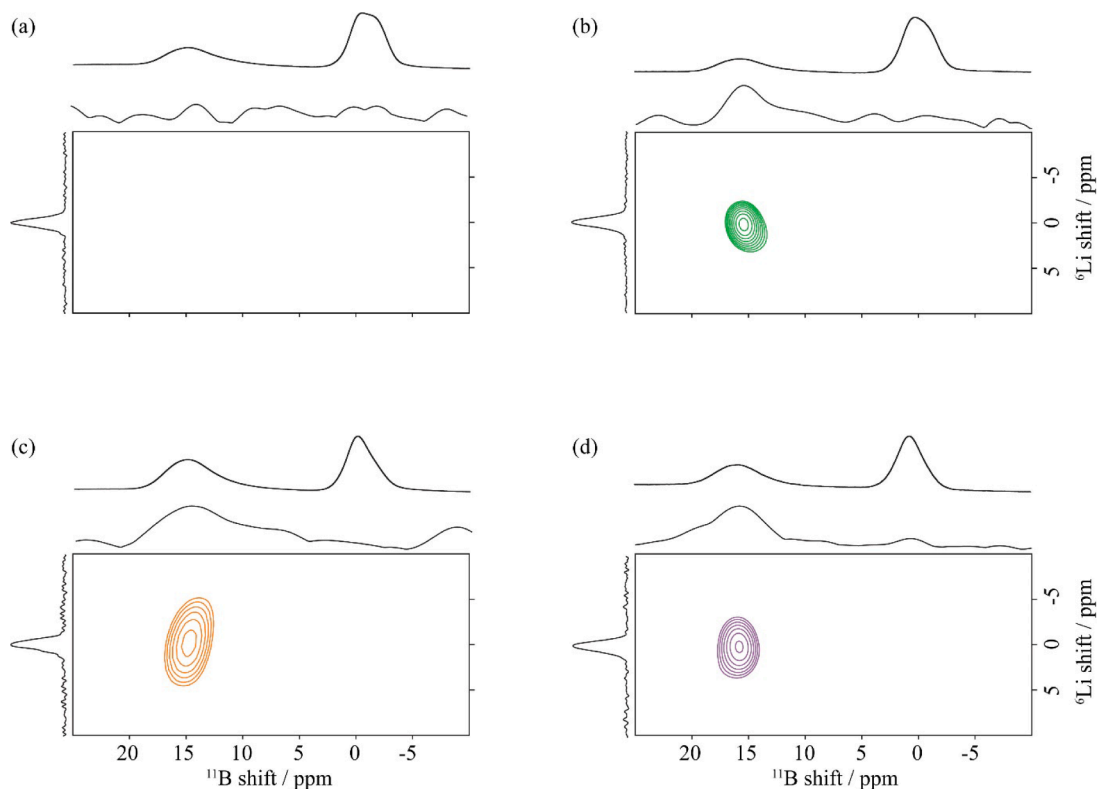

Fig. 6. $^{11}B\{^6Li\}$ J-HMQC spectra of (a) MW ½Li, (b) MW full-Li (green,), (c) CaZn ½Li (orange) and (d) CaZn full-Li (purple) at 850 MHz. The vertical spectra are the 1D ^6Li MAS NMR spectra (Figure S12). The horizontal spectra are the 1D ^{11}B MAS NMR spectra on the top and the internal projections on the bottom.

broader than the 1D ^{6}Li MAS NMR spectra likely due to reduced resolution caused by a small number of t_1 points due to the time-consuming nature of this experiment.

To further examine the association of Li with B sites, ^{11}B{^{6}Li} D-HMQC MAS spectra with a SR4$_1^2$ recoupling sequence were carried out. This experiment reintroduces the dipolar-coupling interaction which is removed under MAS enabling two-dimensional spectra between two quadrupolar nuclei that are close together in space and mediated by dipolar coupling interactions to be obtained. The resulting spectra reveal correlations between the BO$_3$ (15 ppm) signals and Li resonances (0 ppm) for all compositions (Fig. 7); additionally, correlations between the [BO$_4$]$^-$ (0 ppm) and Li resonances are observed for both MW glasses and CaZn full-Li glass, demonstrating spatial proximity between Li and BO$_3$ and [BO$_4$]$^-$ sites depending on composition. No correlation signal between Li [BO$_4$]$^-$ was observed for CaZn ½Li glass which implies there is insufficient Li in the glass network to charge balance these anionic sites or below the sensitivity limit of NMR. Similarly to the J-HMQC results for MW ½Li (Fig. 6a) it is possible that due to the low natural abundance of ^{6}Li the possible Li and [BO$_4$]$^-$ correlations in CaZn full-Li are hidden within the spectral noise. Despite this, the D-HMQC experimental results indicate that Li BO$_3$ interactions occur primarily over Li [BO$_4$]$^-$ as strong correlation signals between Li and BO$_3$ are observed for all compositions.

These results signify a relationship between the amount of Li and B in the glass network with the formation of strong through-space Li [BO$_4$]$^-$ interactions and that Li takes on a charge compensator role with anionic sites such as [BO$_4$]$^-$. The presence of signal between Li and BO$_3$ in the MW ½Li glass observed using the D-HMQC pulse sequence and the corresponding lack of correlating signal from the J-HMQC experiment additionally suggests that Li and BO$_3$ interactions are largely dipolar coupling mediated. This further suggests that NBOs are not created on

the BO$_3$ sites with the addition of lithium (as the J-HMQC spectra of the MW glass may suggest), supported from the ^{11}B MAS NMR which showed an increase in [BO$_4$]$^-$ sites. If NBOs were forming on the BO$_3$ sites, we would not observe an increase in [BO$_4$]$^-$ sites.

Further exploration of the association of Li with anionic sites was carried out from dimensional multinuclear ^{27}Al{^{6}Li} D-HMQC MAS spectra with the SR4$_1^2$ recoupling sequence acquired on the full- and ½Li CaZn glasses (Fig. 8). The resultant spectra exhibit a correlation between the ^{27}Al resonance at 60 ppm and Li resonance (0 ppm) for the CaZn full-Li glass only. The ^{27}Al signal at 60 ppm is characteristic of an Al in tetrahedral coordination with four coordinating oxygens and a net negative charge; that is, [AlO$_4$]$^-$ as discussed previously [24]. No other Al sites were present in the 1D ^{27}Al MAS NMR spectra thus we conclude that Al only exists in tetrahedral coordination in both full- and ½Li CaZn glasses. We have assigned this through-space correlation observed in Fig. 8b to a Li$^+$ [AlO$_4$]$^-$ interaction arising from the charge compensating role of Li$^+$. The absence of signal in the ½Li CaZn glass (Fig. 8a) could be the result of insufficient Li available in the glass network to charge balance anionic sites or perhaps, similarly with the ^{11}B{^{6}Li} HMQC results above for CaZn ½Li and MW ½Li, spatial interactions between ^{27}Al and ^{6}Li is small and lost in the noise due to the low natural abundance of ^{6}Li. Despite this, the results imply that more Li [AlO$_4$]$^-$ spatial interactions occur at higher lithium contents. This enhances the evidence of a relationship between Li concentration and its role as charge compensator in the glass network. To the best of our knowledge, this is the first work to report on the relation of Li's role as charge compensator with the formation of a spatial interaction between Li$^+$ and anionic sites.
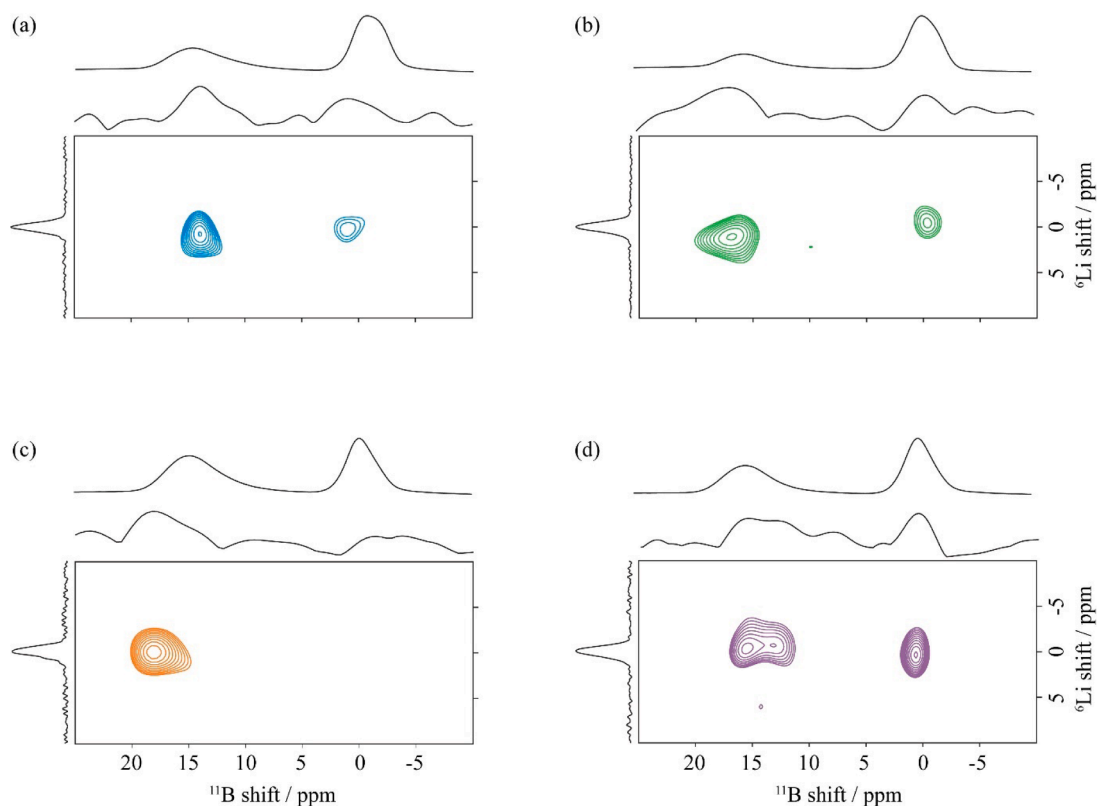

Fig. 7. ^{11}B{^{6}Li} D-HMQC spectra with a SR4$_1^2$ recoupling sequence of (a) MW ½Li, (b) MW full-Li (green,), (c) CaZn ½Li (orange) and (d) CaZn full-Li (purple) at 850 MHz. The vertical spectra are the 1D ^{6}Li MAS NMR spectra (Figure S12). The horizontal spectra are the 1D ^{11}B MAS NMR spectra on the top and the internal projections on the bottom. Note the shoulder at approx. 8 ppm in the internal projection of CaZn full-Li which has been assigned as poor SNR as ^{11}B does not have signal at this shift.
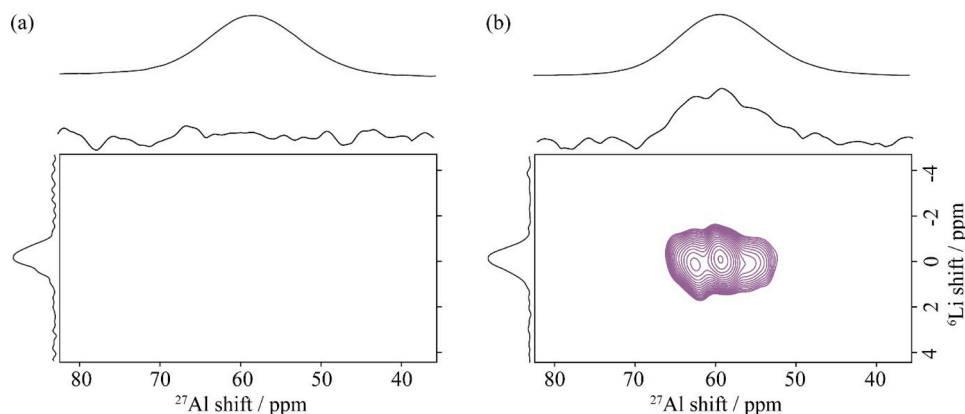
Fig. 8. $^{27}Al\{^6Li\}$ D-HMQC spectra with a SR4_2^1 recoupling sequence of (a) CaZn ½Li and (b) CaZn full-Li (purple) at 850 MHz. The vertical spectra are the 1D ^6Li MAS NMR spectra (Figure S12). The horizontal spectra are the 1D ^{27}Al MAS NMR spectra on top and the internal projections on the bottom.

3.2. Raman spectroscopy

Raman spectra (Figs. 9 and 10) were collected out to probe changes in glass structure due to compositional differences and to complement the NMR data. The Raman spectra of all four glasses investigated here display signals typical of borosilicate glasses, which can be divided into three main regions: region 1 between 200 and 850 cm^{-1} is due to mixed stretching and bending modes of Si-O-Si vibrational units and ring breathing modes of borate or borosilicate ring unit groups [82,84,85], region 2 between 850 and 1250 cm^{-1} to Q^n vibrational units [82,86,87] (Fig. 10 displays magnified views of this region), and region 3 between 1250 and 1600 cm^{-1} to B-O vibrational units [82,88,89]. Note that it is particularly difficult to obtain high quality data in region 3 due to high fluorescence. In the context of this work, the most important Raman bands observed for all glasses are the modes assigned specifically to the Si Q^n units at 940–970 cm^{-1} (Q^2), 1030–1050 cm^{-1} (Q^3) and 1150–1170 cm^{-1} (Q^4) [82,84,86,90,91] which were fitted using Gaussian line-shapes (Fig. 10) to determine the proportion of Q^2, Q^3 and Q^4 units
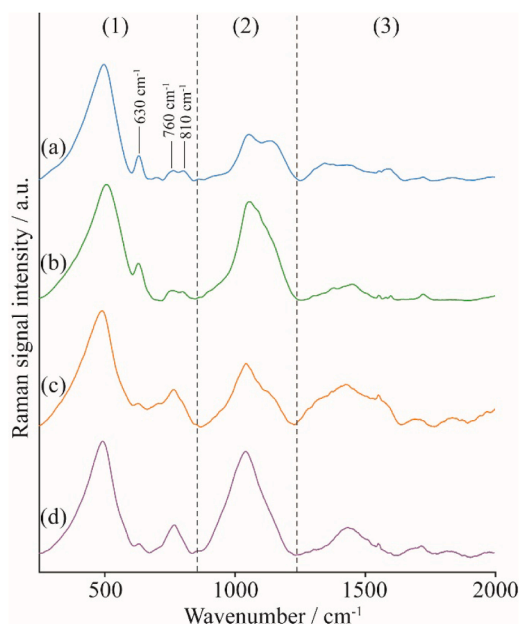
for each composition (Table 3). The percentage of Q^4 units is greater in the ½Li glasses for both MW and CaZn, correlating with the observation in the ^{29}Si NMR spectra. The Q^2 units are least affected by the further addition of Li in both MW and CaZn glasses and it is primarily the transformation of Q^4 to Q^3 units that is observed. The FWHM of the Q^3 site in CaZn full-Li is broader than the other glass compositions suggesting an increase in bond length and/or disorder around the Q^3 sites in this glass network, likely due to the complex nature of this composition.

Although debated in literature [82], the Raman peak at 630 cm^{-1} is likely due to vibrations involving [BO$_4$]$^-$(1B,3Si) sites in danburite-like units from known assignment of similar glass compositions [84,90] and seems to display a larger intensity in the MW glasses compared to CaZn glasses. This agrees with the quantitative ^{11}B MAS NMR data (Table 2) that suggests that the MW glasses also contain the largest concentration of [BO$_4$]$^-$ units. In literature, Raman spectroscopy peaks at 760 and 810 cm^{-1} in borosilicate glasses are typically attributed to four-coordinated and three-coordinated diborate and boroxol rings, respectively [82]. However, in these compositions it is likely the BO$_3$ rings are not boroxol in nature, instead the BO$_3$ ring sites here are likely to be 'modified' ring structures which also contain [BO$_4$]$^-$ [92]. This could explain why the peak at 810 cm^{-1} is better resolved in the MW glasses despite having less BO$_3$ units than the CaZn glasses.

3.3. Thermal analysis

The DSC signals for the second heating cycle (at known cooling/heating rate: 10 K/min) of all four glasses are displayed in Fig. 11. The onset glass transition is characterised by the endothermic inflection and the glass transition temperature was quantified via the tangent and inflection method (Materials and Methods Section) presented in Table 4. DSC measurements were carried out to relate the network connectivity with the thermal properties of the glasses and we found that T$_g$ values are in good agreement with those observed in previous studies for similar glass compositions [93,94]. T$_g$ values decrease with Li content in all glasses, likely due to the depolymerisation role that Li plays in the silicate network. The T$_g$ results for the ½Li MW and CaZn glasses overlap within precision of measurements (796 $\pm$ 6 K and 789 $\pm$ 4 K respectively), as is the case for the full-Li samples (776 $\pm$ 5 K and 771 $\pm$ 4 K respectively), suggesting that the increased complexity afforded by the CaZn glass network does not have a major influence on the T$_g$.

4. Discussion

4.1. The effects of lithium on the borate subnetwork in simple and complex borosilicate glasses

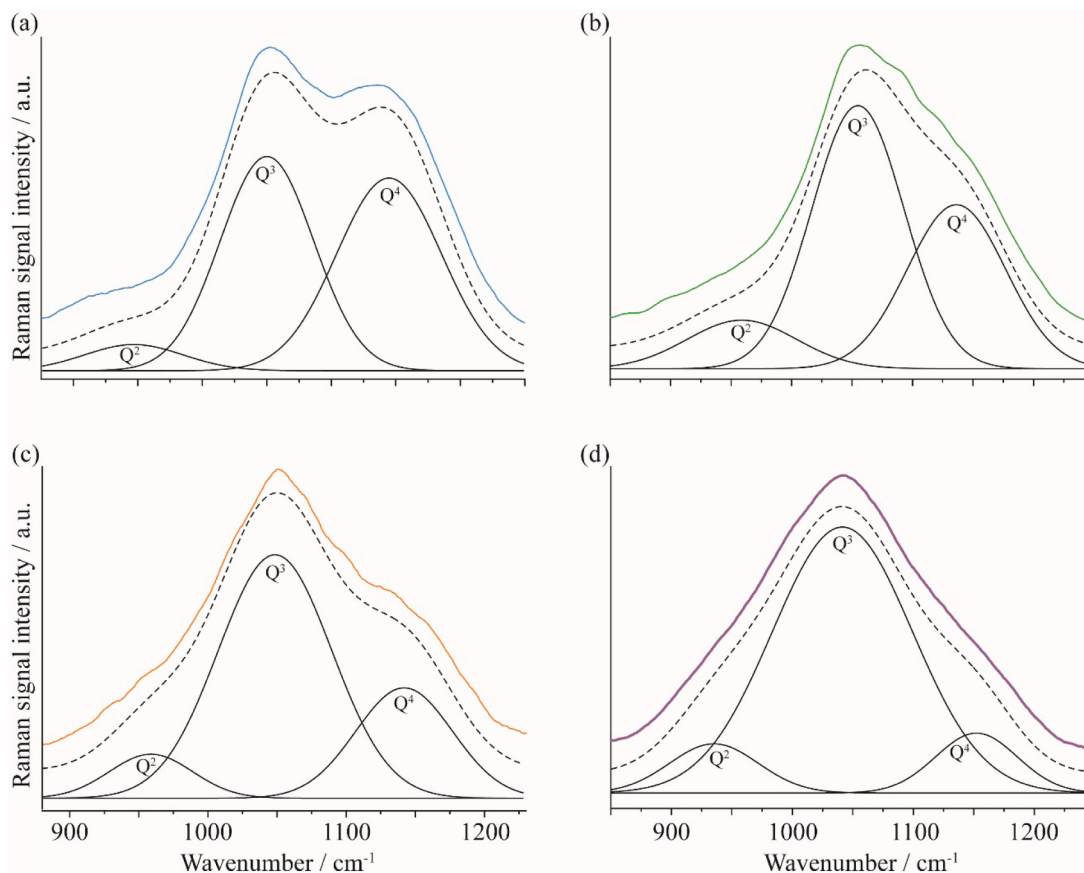The increase in Li content for both the MW and CaZn glasses results

Fig. 9. Comparison of the experimental Raman spectra for (a) MW ½Li (blue), (b) MW full-Li (green), (c) CaZn ½Li (orange) and (d) CaZn full-Li (purple). Data were collected in the range 250 – 2000 cm^{-1}. Regions 1–3 are indicated by vertical dashed lines, modes 630 cm^{-1}, 760 cm^{-1} and 810 cm^{-1} are highlighted as mentioned in the text.

Fig. 10. Comparison of the Si Q^n region (850 - 1250 cm^{-1}) of the Raman spectra for (a) MW ½Li (blue), (b) MW full-Li (green), (c) CaZn ½Li (orange) and (d) CaZn full-Li (purple). The solid-coloured lines are the experimental spectra, the dashed black lines are the total Gaussian fits and the solid black lines are the various Q^n contributions (Table 3).

Table 3
Percentage of the Si Q^2, Q^3 and Q^4 sites in each of the four glass compositions obtained from fitting the Q^n region of the Raman spectra using Gaussian distributions. The errors reported here are a combination of the uncertainty in peak area, FWHM and peak position.

Glass	Q^2 (%)	Q^3 (%)	Q^4 (%)
MW ½Li	6 ± 3	47 ± 3	47 ± 3
MW full-Li	12 ± 3	53 ± 3	35 ± 3
CaZn ½Li	9 ± 3	66 ± 3	25 ± 3
CaZn full-Li	9 ± 3	80 ± 3	11 ± 3

in an increase in [BO$_4$]$^-$ sites at the expense of BO$_3$ sites (Table 2). This conversion is similar in both the MW and CaZn compositions with a slightly enhanced effect in the CaZn glass, with an increase of [BO$_4$]$^-$ sites from 35 % in the ½Li glass to 43 % in the full-Li glass, whereas for MW glass it increases from 60 % to 64 % from the ½Li to the full-Li glass, respectively, and can be attributed to the larger number of BO$_3$ sites present in the 7-oxide CaZn *vs* the 4-oxide MW glasses. As the CaZn glasses have almost half the mol% of Li than their respective MW counterparts (Table 1), it was anticipated that Li would have a reduced effect in the CaZn network which is not observed here. However, when considering the increase in [BO$_4$]$^-$ (1B,3Si), this site experiences the largest percentage increase in both compositions (approx. 11 % in both) thus indicating that Li may have a very similar effect on the 4-oxide and 7-oxide network.

Despite CaZn glass containing Ca^{2+} as an additional network modifier, the mol% of network modifiers in both MW and CaZn glasses remains similar; that is, 15 %, 19 %, 18% and 20 % for MW ½Li, MW full-Li, CaZn ½Li and CaZn full-Li glasses, respectively. The differences in
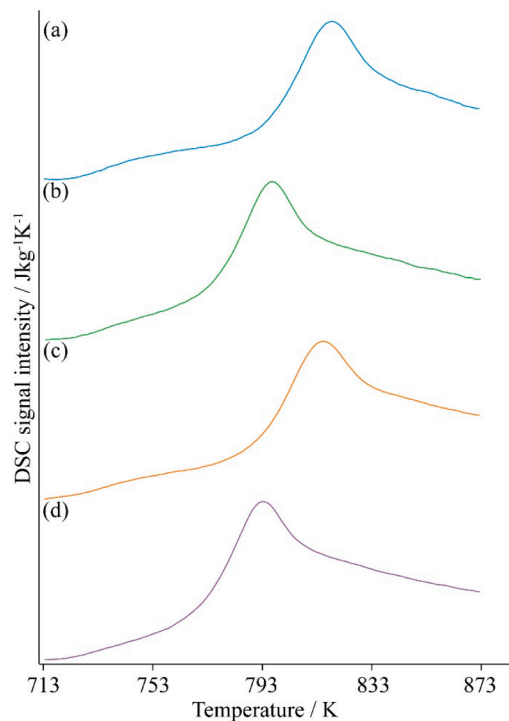

Fig. 11. Comparison of the DSC curves of the second heating cycle of the glass transition temperatures for (a) MW ½Li (blue), (b) MW full-Li (green), (c) CaZn ½Li (orange) and (d) CaZn full-Li (purple) glasses in the range 713–873 K.

Table 4
Glass transition temperatures for each of the four glasses.

Glass	T_g (K)
MW ½Li	796 ± 6
MW full-Li	776 ± 5
CaZn ½Li	789 ± 4
CaZn full-Li	771 ± 4

total percentage of BO_3 and $[BO_4]^-$ sites observed cannot be solely attributed to the presence of Ca^{2+} or the total mol% of network modifiers. The differences can be instead attributed to the additional network formers in the CaZn glass ($[AlO_4]^-$ and $[ZnO_4]^{2-}$) which enhance the connectivity of the glass network as they form linkages with the silicate subnetwork and compete with $[BO_4]^-$ for charge balancing modifiers [25,26]. The depletion of $[BO_4]^-$ in CaZn is thus mainly driven by the competition between anionic sites for charge compensation by the network modifiers and also the avoidance of forming energetically unfavourable ^{4}B-O-^{4}T linkages [95] (where ^{4}B is four-coordinated boron and T=Al or Zn in a 4-fold coordination environment) which could result in charge accumulation. Although the data presented here do not allow for consideration of ^{4}B-O-4 Zn linkages, previous work carried out on Zn containing borosilicate glasses showed that ZnO_4 participates in network formation by linking on average to 2 ± 1 Si Q^4 units via BOs [25]. Other studies on similar glass compositions showed no mention of ^{4}B-O-4 Zn linkages where they observe a higher number of Q^3 species [26] and a decrease in $[BO_4]^-$ sites [96] in Zn containing glasses, in agreement with the data presented here. Similarly, the data presented does not confirm the absence of ^{4}B-O-^{4}Al linkages and it has been shown in the literature that ^{4}B-O-^{4}Al linkages are prominent in aluminoborosilicate glasses with low boron and silicon mixing [97]. However, due to the small amount of Al (~ 3 mol %), high Si-B mixing in the CaZn composition and the avoidance of charge accumulation we do not expect a significant number of ^{4}B-O-^{4}Al in the CaZn glass network [63]. To confirm the presence of ^{4}B-O-^{4}Al linkages rotational-echo double resonance experiments implementing ^{11}B and ^{27}Al nuclei would be required, as has been carried out before in the literature [24,98]. In these experiments it was observed that for borosilicate glasses containing Al, the $[AlO_4]^-$ is in closer proximity to BO_3 than $[BO_4]^-$ due to the Lowenstein's avoidance rule [24]. It is known that $[AlO_4]^-$ units are preferentially charge compensated by Na^+ ions over $[BO_4]^-$, as discussed previously [99] and the addition of Al results in a shift in speciation from anionic $[BO_4]^-$ units to charge-neutral BO_3 units. $[ZnO_4]^{2-}$ structural units will also be in competition for charge compensation [25,100] which may further result in the conversion of $[BO_4]^-$ to BO_3 units in CaZn.

In the MW glass, the percentage of $[BO_4]^-$ sites increases with Li content, which is expected as Li in simple Na borosilicate glasses has previously been found to promote a higher fraction of $[BO_4]^-$ sites, a lower fraction of Si-O-B linkages and a higher fraction of Si-NBOs [20]. The work presented here further shows that the percentage of $[BO_4]^-$ sites increase also with the Si-NBO content in the glass; however, the values reported in Table 2 indicate that the number of Si-O-B linkages increases with Li. Ultimately the findings suggest that the glasses studied herein have a higher degree of Si/B mixing than those previously reported in the literature.

The proximity of Li with BO_3 sites is observed from the ^{11}B{^{6}Li} J-HMQC data (Fig. 6) in both full-Li glasses but only the ½Li CaZn glass, indicating the presence of dipolar and J-coupling interactions between Li BO_3 likely due to BO_3 non-ring sites bonding with Q^3 and Q^2 tetrahedra where Li is acting as network modifier. On the other hand, the association of Li with BO_3 sites is observed from the ^{11}B{^{6}Li} D-HMQC data (Fig. 7) in all glasses, and the association of Li association with $[BO_4]^-$ sites is also observed in both full-Li glasses and ½Li MW glass. These correlation signals indicate the presence of dipolar through-space

interactions in Li BO_3 and Li $[BO_4]^-$. This indicates that when Li acts as network modifier the Li BO_3 interactions formed are J-coupling and dipolar mediated, and when Li is in the charge compensator role the Li $[BO_4]^-$ interactions formed are solely dipolar mediated.

The lack of Li $[BO_4]^-$ correlation signal in the ½Li CaZn glass seems to potentially indicate there are insufficient Li in the glass network to act as charge compensator on anionic sites. This is further evidenced in the ^{27}Al{^{6}Li} D-HMQC spectra (Fig. 8a), where no correlation between Li and $[AlO_4]^-$ was observed for ½Li CaZn glass but a correlation signal was observed for the full-Li CaZn glass. This potentially signifies there is a threshold for the formation of Li and $[BO_4]^-$/$[AlO_4]^-$ spatial interactions, which is governed by Li concentration and the population of anionic sites in the glass network.

In contrast a correlation signal between Li and BO_3 was observed in all glasses (Fig. 7) suggesting that even at low Li_2O contents (as low as 2.2 mol% in this work) Li BO_3 interactions will form in MW and CaZn glass. This is evidence for Li BO_3 spatial interactions forming more readily than both Li $[BO_4]^-$ and Li $[AlO_4]^-$ signifying Li's preference to associate with NBOs over BOs. This behaviour is due to the small ionic radius and large CFS of Li which favours its ability to compete for charge compensation in NBOs.

The slightly larger than average C_Q value experimentally obtained for all glass compositions in this work could be due to the close proximity of Li to the non-ring BO_3 sites, Fig. 7. In the past, neutron diffraction experiments along with Monte Carlo simulations were carried out on lithium and sodium borates to assess the structural differences. It was observed that the lithium borates possessed a more disordered random network than the sodium borates which was attributed to the large number of borate configurations in the lithium borate network, compared to a single borate configuration present in the sodium borate [101,102]. Furthermore, ^{11}B MQMAS experiments of lithium and sodium borates observed spectral broadening in the lithium borates which was not present in the sodium [103]. The authors concluded that this indicated that the lithium borates glasses are more structurally disordered on the short-range scale. Thus, the larger C_Q values obtained experimentally in this work could be due to an increase in disorder brought about by the close proximity of lithium to the sites.

4.2. The effect of lithium on the distribution of sodium in the glass network in simple and complex borosilicate glasses

The impact of Li on the Na distribution can be observed in the ^{23}Na MAS NMR spectra of the four glasses (Fig. 4) with the number of potential Na environments arising from charge compensating different anionic species (*i.e.*, BO_4, ZnO_4, AlO_4, Si Q^3 and Si Q^2). The small increase in ^{23}Na δ with Li in the glasses may be attributed to a decrease in the Na-O bond length. Neutron diffraction experiments on sodium silicate glasses recently found that Na-NBO bonds are not shorter than Na-BO bonds [104] but instead have a wider distribution of bond lengths and valences along with a larger coordination number. Therefore, this decrease in Na-O bond length cannot solely be attributed to more Na-NBO bonds in the glass but instead a change in the Na environment brought about by the increase in Si-NBOs at higher Li content. With the increase in $[BO_4]^-$, Si Q^2 and Si Q^3 sites at higher Li contents the local order around Na^+ ions will have contributions from both NBOs and BOs. There is a preference for network modifying cations to associate with NBOs over BOs creating a hierarchy of bond preference throughout the network; smaller cations (larger CFS) are more likely to associate with NBOs than the larger cations as previously discussed [20]. Similarly to Li^+, Na^+ associates with both NBOs and BOs in the glass network but unlike Li^+, Na^+ primarily associates with anionic $[BO_4]^-$ sites. Secondary to this, Na^+ will charge balance the NBOs formed on Si Q^3/Q^2 units, along with Li^+, rationalising the change in the chemical shift in the full-Li glasses.

4.3. The effect of lithium on the silicate subnetwork in simple and complex borosilicate glasses

The analyses of the ^{29}Si MAS NMR and Raman spectra revealed that the addition of Li to both glass networks result in an increase in Si Q^3 at the expense of Q^4 (Table 3) highlighting depolymerisation of the silicate network. It is interesting that the transformation of Si Q^4 to Q^3 units is primarily observed as opposed to Si Q^3 to Q^2. This effect is greater in the CaZn glass, where the percentage of Q^2 sites does not vary with an increase in Li content. Interestingly, in the MW glass the percentage of Q^2 sites does marginally increase when there is more Li in the network, perhaps due to the simpler nature of this composition. The overall effect of Li concentration on the depolymerisation of the silicate subnetwork is greater in the CaZn composition where a 12 % increase in Q^3 sites was observed in CaZn compared to a 6 % increase in MW (alongside a decrease of 14 % in Q^4 sites in CaZn and a 12 % decrease in MW). This complements the effect of Li observed on the borate subnetwork of the glasses where Li also had a greater effect on the 7-oxide CaZn over the 4-oxide MW network.

These NMR and Raman spectroscopy results were correlated with T_g measurements, where T_g decreases with Li content, indicative depolymerisation promoted by the Li modifier. Silicon is the main network former of the glass structure and its connectivity heavily influences T_g, despite the increase in $[BO_4]^-$ sites which would typically result in an increase in T_g [105]. The T_g values for MW and CaZn ½Li, and for both full-Li glasses, are within precision of the measurements, suggesting that the degree of polymerisation of the silicate network, as captured by the large difference in Si Q^3 and Si Q^4 concentration (Table 3), does not influence the T_g of these glass networks. Instead, we postulate that Li content has a greater effect on T_g rather than Q^n speciation.

5. Conclusions

We have investigated the effects of Li concentration on the connectivity of 4- and 7-oxide glass networks. Quantitative ^{11}B MAS NMR spectra revealed that an increase in Li concentration increases the percentage of $[BO_4]^-$ sites at the expense of BO_3, attributed to Li taking on the role of charge compensator for anionic sites. Complementary data from ^{11}B{^{6}Li} J- and D-HMQC MAS NMR experiments have shown that at all Li concentrations, Li initially acts as a network modifier, creating NBOs on Q^n sites, and subsequently, as charge compensator for $[BO_4]^-$ sites, if sufficient Li remains in the network. We postulated that the charge compensating role of Li forms strong dipolar interactions with the anionic sites. Through ^{29}Si MAS NMR analysis, we showed that Li creates NBOs primarily on Si Q^4 units (as opposed to Q^3) resulting in the transformation of Q^4 to Q^3 and depolymerisation of the silicate subnetwork. The formation of Si-NBOs upon Li addition was evidenced by an increase in ^{23}Na MAS NMR shift, indicating a reduction in Na-O bond length attributed to the increase in Si-NBO content in the glass network. The depolymerisation of the silicate prompts a decrease in T_g, even though MW and CaZn glasses have similar T_g for a given Li content (despite having contrasting Q^4 unit ratios) highlighting the impact Li content has on the T_g. It was found that the addition of more lithium in the glass network had a more significant impact on the CaZn glass (7-oxide) rather than MW (4-oxide), attributed to the increased network modifiers present in CaZn. To probe the relationship further there is potential for future work to be carried out utilising a ^{29}Si{^{6,7}Li} HMQC to confirm the proximity of Li to Q^n tetrahedra. Furthermore, utilising ^{17}O MQMAS NMR on isotopically labelled ^{17}O glasses would further elucidate the relationship of Li with NBOs and BOs with the potential to calculate the number of NBOs/BOs at various Li concentrations.

CRediT authorship contribution statement

Aine G. Black: Writing – original draft, Visualization, Validation, Project administration, Methodology, Investigation, Formal analysis, Conceptualization. **Alex Scrimshire:** Resources, Methodology, Formal analysis. **Dinu Iuga:** Investigation. **Yan Lavallée:** Writing – review & editing, Investigation. **Kate A. Morrison:** Formal analysis, Investigation. **Paul A. Bingham:** Writing – review & editing, Supervision, Resources. **Tracey Taylor:** Supervision. **Laura Leay:** Writing – review & editing. **Mike T. Harrison:** Writing – review & editing, Supervision, Resources, Funding acquisition, Conceptualization. **Frédéric Blanc:** Writing – review & editing, Validation, Supervision, Project administration, Methodology, Conceptualization. **Maulik K. Patel:** Writing – review & editing, Supervision, Project administration, Funding acquisition, Conceptualization.

Declaration of competing interest

The authors declare that they have no known competing financial interests or personal relationships that could have appeared to influence the work reported in this paper.

Data availability

Research data supporting this work are accessible from the University of Liverpool Research Data Catalogue: 10.17638/datacat.liverpool.ac.uk/2824.

Acknowledgements

Supplementary materials

Supplementary material associated with this article can be found, in the online version, at doi:10.1016/j.jnoncrysol.2024.123234.

References

[1] S. Gin, A. Abdelouas, L.J. Criscenti, W.L. Ebert, K. Ferrand, T. Geisler, M. T. Harrison, Y. Inagaki, S. Mitsui, K.T. Mueller, J.C. Marra, C.G. Pantano, E. M. Pierce, J.V. Ryan, J.M. Schofield, C.I. Steefel, J.D. Vienna, An international initiative on long-term behavior of high-level nuclear waste glass, Mater. Today. 16 (2013) 243–248, https://doi.org/10.1016/j.mattod.2013.06.008.

[2] M.T. Harrison, Vitrification of High Level Waste in the UK, Procedia Mater. Sci. 7 (2014) 10–15, https://doi.org/10.1016/j.mspro.2014.10.003.

[3] M.I. Ojovan, W.E. Lee, S.N. Kalmykov, An Introduction to Nuclear Waste Immobilisation, Elsevier, 2019, https://doi.org/10.1016/C2017-0-03752-7.

[4] S. Nagasaki, S. Nakayama, Radioactive Waste Engineering and Management, Springer, Japan, Tokyo, 2015, https://doi.org/10.1007/978-4-431-55417-2.

[5] Nuclear Decommissioning Authority, Geological Disposal Review of Alternative Radioactive Waste Management Options, 2017.

[6] J.A.C. Marples, The preparation, properties, and disposal of vitrified high level waste from nuclear fuel reprocessing, Glas. Technol. 29 (1988) 230–247.

[7] R. Short, Phase Separation and Crystallisation in UK HLW Vitrified Products, Procedia Mater. Sci. 7 (2014) 93–100, https://doi.org/10.1016/j.mspro.2014.10.013.

[8] A.J. Fisher, M.T. Harrison, N.C. Hyatt, R.J. Hand, C.L. Corkhill, The dissolution of simulant UK Ca/Zn-modified nuclear waste glass: the effect of increased waste loading, MRS Adv 6 (2021) 95–102, https://doi.org/10.1557/s43580-021-00025-0.

[9] M.T. Harrison, The Effect of Composition on Short- and Long-term Durability of UK HLW Glass, Procedia Mater. Sci. 7 (2014) 186–192, https://doi.org/10.1016/j.mspro.2014.10.025.

[10] L.G. Soltay, G.S. Henderson, The structure of lithium-containing silicate and germanate glasses, Can. Mineral. 43 (2005) 1643–1651, https://doi.org/10.2113/gscanmin.43.5.1643.

[11] C.P.E. Varsamis, A. Vegiri, E.I. Kamitsos, Molecular dynamics investigation of lithium borate glasses: Local structure and ion dynamics, Phys. Rev. B - Condens. Matter Mater. Phys. 65 (2002) 1–14, https://doi.org/10.1103/PhysRevB.65.104203.

[12] J. Zhong, P.J. Bray, Change in boron coordination in alkali borate glasses, and mixed alkali effects, as elucidated by NMR, J. Non. Cryst. Solids. 111 (1989) 67–76, https://doi.org/10.1016/0022-3093(89)90425-0.

[13] V. Dua, S.K. Arya, K. Singh, Review on transition metals containing lithium borate glasses properties, applications and perspectives, J. Mater. Sci. 58 (2023) 8678–8699, https://doi.org/10.1007/s10853-023-08567-4.

[14] Y.H. Yun, P.J. Bray, ^{11}B nuclear magnetic resonance studies of $Li_2OB_2O_3$ glasses of high Li_2O content, J. Non. Cryst. Solids. 44 (1981) 227–237, https://doi.org/10.1016/0022-3093(81)90025-9.

[15] H. Maekawa, T. Maekawa, K. Kawamura, T. Yokokawa, The structural groups of alkali silicate glasses determined from ^{29}Si MAS-NMR, J. Non. Cryst. Solids. 127 (1991) 53–64, https://doi.org/10.1016/0022-3093(91)90400-Z.

[16] W.J. Dell, P.J. Bray, S.Z. Xiao, ^{11}B NMR Studies and Structural Modelling of $Na_2O-B_2O_3-SiO_2$ Glasses of High Sodium Content, J. Non. Cryst. Solids. 58 (1983) 1–16.

[17] J.F. Stebbins, Cation sites in mixed-alkali oxide glasses: Correlations of NMR chemical shift data with site size and bond distance, Solid State Ionics 112 (1998) 137–141, https://doi.org/10.1016/s0167-2738(98)00224-0.

[18] L.S. Du, J.F. Stebbins, Site connectivities in sodium aluminoborate glasses: Multinuclear and multiple quantum NMR results, Solid State Nucl. Magn. Reson. 27 (2005) 37–49, https://doi.org/10.1016/j.ssnmr.2004.08.003.

[19] A.C. Lee, S.K. Lee, Network polymerization and cation coordination environments in boron-bearing rhyolitic melts: Insights from ^{17}O, ^{11}B, and ^{27}Al solid-state NMR of sodium aluminoborosilicate glasses with varying boron content, Geochim. Cosmochim. Acta. 268 (2020) 325–347, https://doi.org/10.1016/j.gca.2019.10.010.

[20] L.S. Du, J.F. Stebbins, Site preference and Si/B mixing in mixed-alkali borosilicate glasses: A high-resolution ^{11}B and ^{17}O NMR study, Chem. Mater. 15 (2003) 3913–3921, https://doi.org/10.1021/cm034427r.

[21] L.S. Du, J.F. Stebbins, Solid-state NMR study of metastable immiscibility in alkali borosilicate glasses, J. Non. Cryst. Solids. 315 (2003) 239–255, https://doi.org/10.1016/S0022-3093(02)01604-6.

[22] T.L. Goût, M.T. Harrison, I. Farnan, Impacts of lithium on Magnox waste glass dissolution, J. Non. Cryst. Solids. 517 (2019) 96–105, https://doi.org/10.1016/j.jnoncrysol.2019.04.040.

[23] J.M. Roderick, D. Holland, A.P. Howes, C.R. Scales, Density-structure relations in mixed-alkali borosilicate glasses by ^{29}Si and ^{11}B MAS-NMR, J. Non. Cryst. Solids. 293–295 (2001) 746–751, https://doi.org/10.1016/S0022-3093(01)00784-0.

[24] A. Krishnamurthy, V.K. Michaelis, S. Kroeker, Network Formation in Borosilicate Glasses with Aluminum or Gallium: Implications for Nepheline Crystallization, J. Phys. Chem. C. 125 (2021) 8815–8824, https://doi.org/10.1021/acs.jpcc.1c01262.

[25] N.J. Cassingham, M.C. Stennett, P.A. Bingham, N.C. Hyatt, G. Aquilanti, The Structural Role of Zn in Nuclear Waste Glasses, Int. J. Appl. Glas. Sci. 2 (2011) 343–353, https://doi.org/10.1111/j.2041-1294.2011.00067.x.

[26] H. Zhang, C.L. Corkhill, P.G. Heath, R.J. Hand, M.C. Stennett, N.C. Hyatt, Effect of Zn- and Ca-oxides on the structure and chemical durability of simulant alkali borosilicate glasses for immobilisation of UK high level wastes, J. Nucl. Mater. 462 (2015) 321–328, https://doi.org/10.1016/j.jnucmat.2015.04.016.

[27] D. Holland, B.G. Parkinson, M.M. Islam, A. Duddridge, J.M. Roderick, A. P. Howes, C.R. Scales, NMR insights into wasteforms for the vitrification of high-

[28] level nuclear waste, Appl. Magn. Reson. 32 (2007) 483–497, https://doi.org/10.1007/s00723-007-0038-8.

[28] S. Vaishnav, A.C. Hannon, E.R. Barney, P.A. Bingham, Neutron Diffraction and Raman Studies of the Incorporation of Sulfate in Silicate Glasses, J. Phys. Chem. C. 124 (2020) 5409–5424, https://doi.org/10.1021/acs.jpcc.9b10924.

[29] M.C. Eckersley, P.H. Gaskell, A.C. Barnes, P. Chieux, Structural ordering in a calcium silicate glass, Nature 335 (1988) 525–527, https://doi.org/10.1038/335525a0.

[30] K. Shimoda, Y. Tobu, Y. Shimoikeda, T. Nemoto, K. Saito, Multiple Ca^{2+} environments in silicate glasses by high-resolution ^{43}Ca MQMAS NMR technique at high and ultra-high (21.8 T) magnetic fields, J. Magn. Reson. 186 (2007) 156–159, https://doi.org/10.1016/j.jmr.2007.01.019.

[31] J. Wu, J.F. Stebbins, Effects of cation field strength on the structure of aluminoborosilicate glasses: High-resolution ^{11}B, ^{27}Al and ^{23}Na MAS NMR, J. Non. Cryst. Solids 355 (2009) 556–562, https://doi.org/10.1016/j.jnoncrysol.2009.01.025.

[32] B. Reif, S.E. Ashbrook, L. Emsley, M. Hong, Solid-state NMR spectroscopy, Nat. Rev. Methods Prim. 1 (2021) 2, https://doi.org/10.1038/s43586-020-00002-1.

[33] P. Heitjans, J. Kärger, Diffusion in Condensed Matter, Springer, Berlin Heidelberg, Berlin, Heidelberg, 2005, https://doi.org/10.1007/3-540-30970-5.

[34] A.M. George, J.F. Stebbins, Dynamics of Na in sodium aluminosilicate glasses and liquids, Phys. Chem. Miner. 23 (1996) 526–534, https://doi.org/10.1007/BF00242002.

[35] S.L. Tagg, R.E. Youngman, J.W. Zwanziger, Structure of sodium tellurite glasses. Sodium cation environments from sodium-23 NMR, J. Phys. Chem. 99 (1995) 5111–5116, https://doi.org/10.1021/j100014a035.

[36] A.M. George, S. Sen, J.F. Stebbins, ^{23}Na chemical shifts and local structure in crystalline, glassy, and molten sodium borates and germanates, Solid State Nucl. Magn. Reson. 10 (1997) 9–17.

[37] L.S. Du, J.F. Stebbins, Nature of silicon-boron mixing in sodium borosilicate glasses: A high-resolution ^{11}B and ^{17}O NMR study, J. Phys. Chem. B. 107 (2003) 10063–10076, https://doi.org/10.1021/jp034048l.

[38] G. Tricot, J. Trébosc, F. Pourpoint, R. Gauvin, L. Delevoye, The D-HMQC MAS-NMR Technique: An Efficient Tool for the Editing of Through-Space Correlation Spectra Between Quadrupolar and Spin-1/2 (^{31}P, ^{29}Si, ^{1}H, ^{13}C) Nuclei, 1st ed., Elsevier, 2014 https://doi.org/10.1016/B978-0-12-800185-1.00004-8.

[39] D. Iuga, C. Morais, Z. Gan, D.R. Neuville, L. Cormier, D. Massiot, NMR heteronuclear correlation between quadrupolar nuclei in solids, J. Am. Chem. Soc. 127 (2005) 11540–11541, https://doi.org/10.1021/ja052452n.

[40] T.L. Goût, M.T. Harrison, I. Farnan, Relating Magnox and international waste glasses, J. Non. Cryst. Solids. 524 (2019) 119647, https://doi.org/10.1016/j.jnoncrysol.2019.119647.

[41] A.J. Fisher, H. Ding, P. Rajbhandari, B. Walkley, L.R. Blackburn, M.C. Stennett, R. J. Hand, N.C. Hyatt, M.T. Harrison, C.L. Corkhill, Chemical structure and dissolution behaviour of CaO and ZnO containing alkali-borosilicate glass, Mater. Adv. 3 (2022) 1747–1758, https://doi.org/10.1039/d1ma01029h.

[42] L. Takacs, J.S. McHenry, Temperature of the milling balls in shaker and planetary mills, J. Mater. Sci. 41 (2006) 5246–5249, https://doi.org/10.1007/s10853-006-0312-4.

[43] E.A. Leone, S. Curran, M.E. Kotun, G. Carrasquillo, R. van Weeren, S.C. Danforth, Solid-State ^{29}Si NMR Analysis of Amorphous Silicon Nitride Powder, J. Am. Ceram. Soc. 79 (1996) 513–517, https://doi.org/10.1111/j.1151-2916.1996.tb08156.x.

[44] M.E. Smith, E.R.H.H. Van Eck, Recent advances in experimental solid state NMR methodology for half-integer spin quadrupolar nuclei, Prog. Nucl. Magn. Reson. Spectrosc. 34 (1999) 159–201, https://doi.org/10.1016/S0079-6565(98)00028-4.

[45] D. Massiot, F. Fayon, M. Capron, I. King, S. Le Calve, B. Alonso, J.-O. Durand, B. Bujoli, Z. Gan, G. Hoatson, Modelling one- and two-dimensional solid-state NMR spectra, Magn. Reson. Chem. 40 (2002) 70–76.

[46] A. Medek, L. Marinelli, L. Frydman, Multiple-quantum magic-angle spinning NMR of half-integer quadrupolar nuclei, ACS Symp. Ser. (1999) 136–155, https://doi.org/10.1021/bk-1999-0717.ch002.

[47] A. Medek, J.S. Harwood, L. Frydman, Multiple-quantum magic-angle spinning NMR: a new method for the study of quadrupolar nuclei in solids, J. Am. Chem. Soc. 117 (1995) 12779–12787, https://doi.org/10.1021/ja00156a015.

[48] P.J. Grandinetti, J.H. Baltisberger, A. Llor, Y.K. Lee, U. Werner, M.A. Eastman, A. Pines, Pure-absorption-mode lineshapes and sensitivity in two-dimensional dynamic-angle spinning NMR, J. Magn. Reson. 103 (1993) 72–81.

[49] D. Massiot, B. Touzo, D. Trumeau, J.P. Coutures, J. Virlet, P. Florian, P. J. Grandinetti, Two-dimensional magic-angle spinning isotropic reconstruction sequences for quadrupolar nuclei, Solid State Nucl. Magn. Reson. 6 (1996) 73–83, https://doi.org/10.1016/0926-2040(95)01210-9.

[50] A. Brinkmann, A.P.M. Kentgens, Proton-selective ^{17}O-^{1}H distance measurements in fast magic-angle-spinning solid-state NMR spectroscopy for the determination of hydrogen bond lengths, J. Am. Chem. Soc. 128 (2006) 14758–14759, https://doi.org/10.1021/ja065415k.

[51] D. Iuga, A.P.M. Kentgens, Influencing the satellite transitions of half-integer quadrupolar nuclei for the enhancement of magic angle spinning spectra, J. Magn. Reson. 158 (2002) 65–72, https://doi.org/10.1016/S1090-7807(02)00061-7.

[52] H.T. Kwak, P. Srinivasan, J. Quine, D. Massiot, Z. Gan, Satellite transition rotational resonance of homonuclear quadrupolar spins: Magic-angle effect on spin-echo decay and inversion recovery, Chem. Phys. Lett. 376 (2003) 75–82, https://doi.org/10.1016/S0009-2614(03)00958-8.

[53] R.K. Harris, E.D. Becker, S.M.C.D.E. Menezes, R. Goodfellow, P. Granger, NMR Nomenclature, Nuclear Spin Properties and Coventions for Chemical Shifts, J. Pure Appl. Chem. 73 (2001) 1795–1818.

[54] E. Lippmaa, M. Mägi, A. Samoson, M. Tarmak, G. Engelhardt, Investigation of the Structure of Zeolites by Solid-State High-Resolution ^{29}Si NMR Spectroscopy, J. Am. Chem. Soc. 103 (1981) 4992–4996, https://doi.org/10.1021/ja00407a002.

[55] M.R. Schilling, The Glass Transition of Materials Used in Conservation, Stud. Convservation. 34 (1989) 110–116.

[56] R. Youngman, NMR Spectroscopy in Glass Science: A Review of the Elements, Materials (Basel) 11 (2018) 476, https://doi.org/10.3390/ma11040476.

[57] F. Angeli, T. Charpentier, D. de Ligny, C. Cailleteau, Boron Speciation in Soda-Lime Borosilicate Glasses Containing Zirconium, J. Am. Ceram. Soc. 93 (2010) 2693–2704.

[58] F. Angeli, T. Charpentier, M. Gaillard, P. Jollivet, Influence of zirconium on the structure of pristine and leached soda-lime borosilicate glasses: Towards a quantitative approach by ^{17}O MQMAS NMR, J. Non. Cryst. Solids. 354 (2008) 3713–3722, https://doi.org/10.1016/j.jnoncrysol.2008.03.046.

[59] S. Kroeker, J.F. Stebbins, Three-coordinated boron-11 chemical shifts in borates, Inorg. Chem. 40 (2001) 6239–6246, https://doi.org/10.1021/ic010305u.

[60] L. Züchner, J.C.C. Chan, W. Müller-Warmuth, H. Eckert, Short-range order and site connectivities in sodium aluminoborate glasses: i. quantification of local environments by high-resolution ^{11}B, ^{23}Na, and ^{27}Al Solid-State NMR, J. Phys. Chem. B. 102 (1998) 4495–4506, https://doi.org/10.1021/jp980587s.

[61] S. Soudani, M. Paris, Y. Morizet, Influence of high-pressure on the short-range structure of Ca or Na aluminoborosilicate glasses from 11B and 27Al solid-state NMR, J. Non. Cryst. Solids. 638 (2024) 123085, https://doi.org/10.1016/j.jnoncrysol.2024.123085.

[62] A.C. Lee, S.K. Lee, Effect of composition on structural evolution and NMR parameters of quadrupolar nuclides in sodium borate and aluminoborosilicate glasses: a view from high-resolution ^{11}B, ^{27}Al, and ^{17}O solid-state NMR, J. Non. Cryst. Solids. 555 (2021) 120271, https://doi.org/10.1016/j.jnoncrysol.2020.120271.

[63] L.S. Du, J.F. Stebbins, Network connectivity in aluminoborosilicate glasses: A high-resolution ^{11}B, ^{27}Al and ^{17}O NMR study, J. Non. Cryst. Solids. 351 (2005) 3508–3520, https://doi.org/10.1016/j.jnoncrysol.2005.08.033.

[64] V.K. Michaelis, P.M. Aguiar, S. Kroeker, Probing alkali coordination environments in alkali borate glasses by multinuclear magnetic resonance, J. Non. Cryst. Solids. 353 (2007) 2582–2590, https://doi.org/10.1016/j.jnoncrysol.2007.04.029.

[65] A. Dhara, R.K. Mishra, R. Shukla, T.P. Valsala, V. Sudarsan, A.K. Tyagi, C. P. Kaushik, A comparative study on the structural aspects of sodium borosilicate glasses and barium borosilicate glasses: Effect of Al$_2$O$_3$ addition, J. Non. Cryst. Solids. 447 (2016) 283–289, https://doi.org/10.1016/j.jnoncrysol.2016.04.040.

[66] M. Storek, M. Adjei-Acheamfour, R. Christensen, S.W. Martin, R. Böhmer, Positive and Negative Mixed Glass Former Effects in Sodium Borosilicate and Borophosphate Glasses Studied by ^{23}Na NMR, J. Phys. Chem. B. 120 (2016) 4482–4495, https://doi.org/10.1021/acs.jpcb.6b00482.

[67] G. Czjzek, J. Fink, F. Götz, H. Schmidt, Atomic coordination and the distribution ofelectric field gradients in amorphous solids, Phys. Rev. B - Condens. Matter Mater. Phys. 23 (1981).

[68] J.B. d'Espinose de Lacaillerie, C. Fretigny, D. Massiot, MAS NMR spectra of quadrupolar nuclei in disordered solids: The Czjzek model, J. Magn. Reson. 192 (2008) 244–251, https://doi.org/10.1016/j.jmr.2008.03.001.

[69] U. Werner-Zwanziger, A.L. Paterson, J.W. Zwanziger, The Czjzek distribution in solid-state NMR: Scaling properties of central and satellite transitions, J. Non. Cryst. Solids. 550 (2020) 120383, https://doi.org/10.1016/j.jnoncrysol.2020.120383.

[70] S.K. Lee, J.F. Stebbins, The distribution of sodium ions in aluminosilicate glasses: A high-field Na-23 MAS and 3Q MAS NMR study, Geochim. Cosmochim. Acta. 67 (2003) 1699–1709, https://doi.org/10.1016/S0016-7037(02)00026-7.

[71] F. Angeli, O. Villain, S. Schuller, S. Ispas, T. Charpentier, Insight into sodium silicate glass structural organization by multinuclear NMR combined with first-principles calculations, Geochim. Cosmochim. Acta. 75 (2011) 2453–2469, https://doi.org/10.1016/j.gca.2011.02.003.

[72] M.C. Davis, D.C. Kaseman, S.M. Parvani, K.J. Sanders, P.J. Grandinetti, D. Massiot, P. Florian, Q$^{(n)}$ species distribution in K$_2$O.2SiO$_2$ glass by ^{29}Si magic angle flipping NMR, J. Phys. Chem. A. 114 (2010) 5503–5508, https://doi.org/10.1021/jp100530m.

[73] E. Schneider, J.F. Stebbins, A. Pines, Speciation and local structure in alkali and alkaline earth silicate glasses: Constraints from ^{29}Si NMR spectroscopy, J. Non. Cryst. Solids. 89 (1987) 371–383, https://doi.org/10.1016/S0022-3093(87)80279-X.

[74] T. Charpentier, S. Ispas, M. Profeta, F. Mauri, C.J. Pickard, First-Principles Calculation of ^{17}O, ^{29}Si, and ^{23}Na NMR Spectra of Sodium Silicate Crystals and Glasses, J. Phys. Chem. B. 108 (2004) 4147–4161, https://doi.org/10.1021/jp0367225.

[75] T. Nanba, M. Nishimura, Y. Miura, A theoretical interpretation of the chemical shift of ^{29}Si NMR peaks in alkali borosilicate glasses, Geochim. Cosmochim. Acta. 68 (2004) 5103–5111, https://doi.org/10.1016/j.gca.2004.05.042.

[76] G. Calas, L. Cormier, L. Galoisy, P. Jollivet, Structure-property relationships in multicomponent oxide glasses, Comptes Rendus Chim 5 (2002) 831–843, https://doi.org/10.1016/S1631-0748(02)01459-5.

[77] J.W. MacKenzie, A. Bhatnagar, D. Bain, S. Bhowmik, C. Parameswar, K. Budhwani, S.A. Feller, M.L. Royle, S.W. Martin, ^{29}Si MAS-NMR study of the short range order in alkali borosilicate glasses, J. Non. Cryst. Solids. 177 (1994) 269–276, https://doi.org/10.1016/0022-3093(94)90540-1.

[78] S.W. Martin, Recent advances in the study of fast ionically conducting glasses using nuclear magnetic resonance techniques, Mater. Chem. Phys. 23 (1989) 225–265, https://doi.org/10.1016/0254-0584(89)90026-6.

[79] S.W. Martin, D. Bain, K. Budhwani, S. Feller, ^{29}Si MAS-NMR Study of the Short-Range Order in Lithium Borosilicate Glasses, J. Am. Ceram. Soc. 75 (1992) 1117–1122, https://doi.org/10.1111/j.1151-2916.1992.tb05547.x.

[80] A.J. Pell, G. Pintacuda, C.P. Grey, Paramagnetic NMR in solution and the solid state, Prog. Nucl. Magn. Reson. Spectrosc. 111 (2019) 1–271, https://doi.org/10.1016/j.pnmrs.2018.05.001.

[81] D. Massiot, F. Fayon, B. Alonso, J. Trebosc, J.P. Amoureux, Chemical bonding differences evidenced from J-coupling in solid state NMR experiments involving quadrupolar nuclei, J. Magn. Reson. 164 (2003) 160–164, https://doi.org/10.1016/S1090-7807(03)00134-4.

[82] D. Manara, A. Grandjean, D.R. Neuville, Advances in understanding the structure of borosilicate glasses: A raman spectroscopy study, Am. Mineral 94 (2009) 777–784, https://doi.org/10.2138/am.2009.3027.

[83] S. Prasad, T.M. Clark, T.H. Sefzik, H.T. Kwak, Z. Gan, P.J. Grandinetti, Solid-state multinuclear magnetic resonance investigation of Pyrex®, J. Non. Cryst. Solids. 352 (2006) 2834–2840, https://doi.org/10.1016/j.jnoncrysol.2006.02.085.

[84] P. Rautiyal, G. Gupta, R. Edge, L. Leay, A. Daubney, M.K. Patel, A.H. Jones, P. A. Bingham, Gamma irradiation-induced defects in borosilicate glasses for high-level radioactive waste immobilisation, J. Nucl. Mater. 544 (2021) 152702, https://doi.org/10.1016/j.jnucmat.2020.152702.

[85] D.W. Matson, S.K. Sharma, J.A. Philpotts, The structure of high-silica alkali-silicate glasses. A Raman spectroscopic investigation, J. Non. Cryst. Solids. 58 (1983) 323–352, https://doi.org/10.1016/0022-3093(83)90032-7.

[86] B.O. Mysen, J.D. Frantz, Raman spectroscopy of silicate melts at magmatic temperatures: Na$_2$O-SiO$_2$, K$_2$O-SiO$_2$ and Li$_2$O-SiO$_2$ binary compositions in the temperature range 25-1475°C, Chem. Geol. 96 (1992) 321–332, https://doi.org/10.1016/0009-2541(92)90062-A.

[87] B.O. Mysen, J.D. Frantz, Silicate melts at magmatic temperatures: in-situ structure determination to 1651°C and effect of temperature and bulk composition on the mixing behavior of structural units, Contrib. to Mineral. Petrol. 117 (1994) 1–14, https://doi.org/10.1007/BF00307725.

[88] B.N. Meera, A.K. Sood, N. Chandrabhas, J. Ramakrishna, Raman study of lead borate glasses, J. Non. Cryst. Solids. 126 (1990) 224–230, https://doi.org/10.1016/0022-3093(90)90823-5.

[89] B. Boizot, G. Petite, D. Ghaleb, B. Reynard, G. Calas, Raman study of Beta-irradiated glasses, J. Non. Cryst. Solids. 243 (1999) 268–272.

[90] B.G. Parkinson, D. Holland, M.E. Smith, C. Larson, J. Doerr, M. Affatigato, S. A. Feller, A.P. Howes, C.R. Scales, Quantitative measurement of Q^3 species in silicate and borosilicate glasses using Raman spectroscopy, J. Non. Cryst. Solids. 354 (2008) 1936–1942, https://doi.org/10.1016/j.jnoncrysol.2007.06.105.

[91] O.J. McGann, P.A. Bingham, R.J. Hand, A.S. Gandy, M. Kavčič, M. Žitnik, K. Bučar, R. Edge, N.C. Hyatt, The effects of γ-radiation on model vitreous wasteforms intended for the disposal of intermediate and high level radioactive wastes in the United Kingdom, J. Nucl. Mater. 429 (2012) 353–367, https://doi.org/10.1016/j.jnucmat.2012.04.007.

[92] J. Wu, J.F. Stebbins, Quench rate and temperature effects on boron coordination in aluminoborosilicate melts, J. Non. Cryst. Solids. 356 (2010) 2097–2108, https://doi.org/10.1016/j.jnoncrysol.2010.08.015.

[93] V.K. Deshpande, A.P. Raut, Effect of gamma irradiation on the density, glass transition temperature and electrical conductivity of lithium borosilicate glasses with alumina addition, J. Non. Cryst. Solids. 457 (2017) 104–110, https://doi.org/10.1016/j.jnoncrysol.2016.11.028.

[94] M.M. Lima, R. Monteiro, Characterisation and thermal behaviour of a borosilicate glass, Thermochim. Acta. 373 (2001) 69–74, https://doi.org/10.1016/S0040-6031(01)00456-7.

[95] W. Loewenstein, M. Lowenstein, The Distribution of Aluminium in the Tetrehedra Of Silicates and Aluminates, Mineral. Soc. Am. 39 (1954) 92–96.

[96] E.R. Vance, D.J. Gregg, I. Karatchevtseva, G.J. Griffiths, K. Olufson, G.J. Rees, J. V. Hanna, The influence of ZnO incorporation on the aqueous leaching characteristics of a borosilicate glass, J. Nucl. Mater. 494 (2017) 37–45, https://doi.org/10.1016/j.jnucmat.2017.06.035.

[97] E.I. Morin, J. Wu, J.F. Stebbins, Modifier cation (Ba, Ca, La, Y) field strength effects on aluminum and boron coordination in aluminoborosilicate glasses: The roles of fictive temperature and boron content, Appl. Phys. A Mater. Sci. Process 116 (2014) 479–490, https://doi.org/10.1007/s00339-014-8369-4.

[98] M. Bertmer, L. Züchner, J.C.C. Chan, H. Eckert, Short and medium range order in sodium aluminoborate glasses. 2. Site connectivities and cation distributions studied by rotational echo double resonance NMR spectroscopy, J. Phys. Chem. B. 104 (2000) 6541–6553, https://doi.org/10.1021/jp9941918.

[99] Q.J. Zheng, R.E. Youngman, C.L. Hogue, J.C. Mauro, M. Potuzak, M. M. Smedskjaer, Y.Z. Yue, Structure of boroaluminosilicate glasses: Impact of [Al$_2$O$_3$]/[SiO$_2$] ratio on the structural role of sodium, Phys. Rev. B - Condens. Matter Mater. Phys. 86 (2012) 1–12, https://doi.org/10.1103/PhysRevB.86.054203.

[100] M.Le Grand, A.Y. Ramos, G. Calas, L. Galoisy, D. Ghaleb, F. Pacaud, Zinc environment in aluminoborosilicate glasses by Zn K-edge extended x-ray absorption fine structure spectroscopy, J. Mater. Res. 15 (2000) 2015–2019, https://doi.org/10.1557/JMR.2000.0289.

[101] J. Swenson, L. Börjesson, W.S. Howells, Structure of fast ion conducting borate glasses by neutron diffraction and reverse Monte Carlo simulations, Phys. Scr. T57 (1995) 117–121, https://doi.org/10.1088/0031-8949/1995/T57/020.

[102] J. Swenson, L. Börjesson, W.S. Howells, Structure of borate glasses from neutron-diffraction experiments, Phys. Rev. B. 52 (1995) 9310–9319, https://doi.org/10.1103/PhysRevB.52.9310.

[103] P.M. Aguiar, S. Kroeker, Boron speciation and non-bridging oxygens in high-alkali borate glasses, J. Non. Cryst. Solids. 353 (2007) 1834–1839, https://doi.org/10.1016/j.jnoncrysol.2007.02.013.

[104] A.C. Hannon, S. Vaishnav, O.L.G. Alderman, P.A. Bingham, The structure of sodium silicate glass from neutron diffraction and modeling of oxygen-oxygen correlations, J. Am. Ceram. Soc. 104 (2021) 6155–6171, https://doi.org/10.1111/jace.17993.

[105] T. Rouxel, Elastic Properties and Short-to Medium-Range Order in Glasses, J. Am. Ceram. Soc. 90 (2007) 3019–3039.